RAPID RELAXATION-BASED COLOR MAGNETIC PARTICLE IMAGING

A DISSERTATION SUBMITTED TO
THE GRADUATE SCHOOL OF ENGINEERING AND SCIENCE
OF BILKENT UNIVERSITY
IN PARTIAL FULFILLMENT OF THE REQUIREMENTS FOR
THE DEGREE OF
DOCTOR OF PHILOSOPHY
IN
ELECTRICAL AND ELECTRONICS ENGINEERING

By
Musa Tunç Arslan
September 2022

Rapid Relaxation-Based Color Magnetic Particle Imaging
By Musa Tunç Arslan
September 2022

We certify that we have read this dissertation and that in our opinion it is fully adequate, in scope and in quality, as a dissertation for the degree of Doctor of Philosophy.

Emine Ülkü Sarıtaş Çukur(Advisor)

Tolga Çukur

Sevinç Figen Öktem

Ahmet Enis Çetin

Ergin Atalar

Approved for the Graduate School of Engineering and Science:

Orhan Arıkan
Director of the Graduate School

ABSTRACT

RAPID RELAXATION-BASED COLOR MAGNETIC PARTICLE IMAGING

Musa Tunç Arslan
Ph.D. in Electrical and Electronics Engineering
Advisor: Emine Ülkü Sarıtaş Çukur
September 2022

Magnetic particle imaging (MPI) is a rapidly developing medical imaging modality that exploits the non-linear response of magnetic nanoparticles (MNPs). Color MPI widens the functionality of MPI, empowering it with the capability to distinguish different MNPs and/or MNP environments. The system function approach for color MPI relies on extensive calibrations that capture the differences in the harmonic responses of the MNPs. An alternative calibration-free x-space-based method called TAURUS (TAU estimation via Recovery of Underlying mirror Symmetry) estimates a map of the relaxation time constant, τ, by recovering the underlying mirror symmetry in the MPI signal. However, TAURUS requires a back and forth scanning of a given region, restricting its usage to slow trajectories with constant or piecewise constant focus fields (FFs). In this thesis, a novel technique is proposed to increase the performance of TAURUS and enable τ map estimation for rapid and multi-dimensional trajectories. The proposed technique is based on correcting the distortions on mirror symmetry induced by time-varying FFs. Simulations and experiments in an in-house MPI scanner demonstrates that the proposed method successfully estimates high-fidelity τ maps for rapid trajectories that provide orders of magnitude reduction in scanning time (over 300 fold for simulations and over 8 fold for experiments) while preserving the calibration-free property of TAURUS. Additionally, the proposed method can successfully map the effective relaxation time constants in a relatively wide field-of-view at frame rates exceeding 5 frames-per-second. This thesis presents the first simulation results demonstrating that the proposed method is capable of generating high fidelity and high frame-rate color MPI images in real time.

Keywords: Magnetic particle imaging, color MPI, nanoparticle relaxation, mirror symmetry, x-space MPI, rapid trajectory.

ÖZET

HIZLI RELAKSASYON-TABANLI RENKLİ MANYETİK PARÇACIK GÖRÜNTÜLEME

Musa Tunç Arslan
Elektrik ve Elektronik Mühendisliği, Doktora
Tez Danışmanı: Emine Ülkü Sarıtaş Çukur
Eylül 2022

Manyetik parçacık görüntüleme (MPG), manyetik nanoparçacıkların (MNP) doğrusal olmayan tepkisinden yararlanan, hızla gelişen bir tıbbi görüntüleme yöntemidir. Renkli MPG, MPG'nin işlevselliğini genişleterek, onu farklı MNP'leri ve/veya MNP ortamlarını ayırt etme yeteneği ile güçlendirir. Renkli MGP için sistem fonksiyonu yaklaşımı MNP'lerin harmonik tepkilerindeki farklılıkları yakalayan kapsamlı kalibrasyonlara dayanır. TAURUS (altta yatan ayna simetrisinin geri kazanılması ile TAU tahmini) isimli alternatif bir kalibrasyonsuz x-uzayı tabanlı yöntem, MPG sinyalinin altında yatan ayna simetrisini geri kazanarak relaksasyon zaman sabiti τ'nun bir haritasını tahmin eder. Ancak, TAURUS bir bölgenin ileri geri taramasını gerektirdiğinden, kullanımı sabit veya parçalı sabit odaklanma alanlı (OA), yavaş gezingelerle sınırlıdır. Bu tezde, TAURUS'un performansını artırmak, hızlı ve çok boyutlu gezingeler için τ harita tahminine olanak sağlamak amacıyla yeni bir teknik önerilmiştir. Önerilen teknik, zamanla değişen OA'lardan kaynaklı ayna simetrisindeki bozulmaların düzeltilmesine dayanmaktadır. Simülasyonlar ve kurum içi MPG tarayıcısındaki deneyler, önerilen yöntemin, TAURUS'un kalibrasyon gerektirmeyen özelliğini korurken tarama süresinde büyük düşüşler sağlayan (simülasyonlar için 300 katın üzerinde ve deneyler için 8 katın üzerinde) hızlı gezingeler için yüksek doğruluklu τ haritalarını başarılı bir şekilde tahmin ettiğini göstermektedir. Ek olarak, önerilen yöntem, saniyede 5 kareyi geçen hızlarda görece geniş bir görüş alanı için etkin relaksasyon zaman sabitlerini başarılı bir şekilde haritalayabilir. Bu tez, önerilen yöntemin gerçek zamanlı olarak yüksek doğrulukta ve yüksek kare hızlı renkli MPI görüntüleri üretebildiğini gösteren ilk simülasyon sonuçlarını sunmaktadır.

Anahtar sözcükler: Manyetik parçacık görüntüleme, renkli MPG, nanoparçacık relaksasyonu, ayna simetrisi, x-uzayı MPG, hızlı gezinge.

Acknowledgement

First of all, I would like to thank my thesis advisor, Emine Ülkü Sarıtaş. I met her during my doctoral studies while taking her various courses. Her deep knowledge, lecturing, and respectful and caring way of interacting with students were the primary reasons for my desire to work with her. This approach of hers toward me increasingly continued throughout my doctoral education. I have experienced that she is very caring and understanding towards her students and her academic guidance is very accurate. I wish I had started working with her sooner. I cannot thank her enough for her support, help, and understanding during this challenging process. I hope to achieve work in line with her standards in my future career.

I would like to thank Tolga Çukur and Figen Sevinç Öktem for being on my thesis committee and for their valuable comments and suggestions throughout this process. Additionally, I would like to thank Ergin Atalar and Ahmet Enis Çetin for taking the time to be on my Ph.D. dissertation defense committee.

I would like to thank the following funding agencies for supporting the work in this thesis: the Scientific and Technological Research Council of Turkey through TUBITAK Grants 120E208 and 217S069.

I would also like to thank my former colleagues Cenk Ertürk, Erdinç Atılgan, Onur Yorulmaz and my colleagues in the Meteksan Defense Industry Communication Systems System Engineering group Özgür Taşoğlu, İnanç Yıldız, Metehan Zengin and Erem Erdem. During the time I spent with them, their mind-opening and entertaining conversations helped me keep my morale and self-confidence high. I started working with them in a formal company environment for the first time, and I would like to state that this time we spent together was a very good experience for me. I would like to thank them for their friendship. I would especially like to thank Cenk Ertürk, Erdinç Atılgan, and Onur Yorulmaz for showing me different aspects of electronic engineering that I have not seen before and broadening my horizons. The concepts they introduced to me have their tracers in my work and increased the quality of it.

I would like to thank Dr. Mustafa Ütkür for his valuable discussions and

feedback during my short friendship with him, for his useful ideas, and for introducing me to magnetic particle imaging equipment in our laboratory early on in UMRAM.

I would also like to thank Cem Işık Doğru for his valuable friendship and entertaining conversations. I enjoyed our discussions on economics, politics, history, and all other aspects of life. Going to a bookstore together and criticizing art and literature will always be enjoyable. I firmly believe we learned a lot from each other.

I would like to thank my mother, father, and especially my sister Gülce for their support during the difficult periods of my doctoral education, for trying to help me under all circumstances, and for listening to me. I think I would not have been able to complete this process without their moral support in my difficult times or if they had not shared my joy in my happy times. I think everyone needs such a family, and I see myself privileged for having it.

Contents

List of Figures

Chapter 1

Introduction

Medical imaging has been dominated by anatomical imaging methods, such as x-ray, computed tomography (CT), ultrasound (US), and magnetic resonance imaging (MRI). Different signal origins are often of interest in medical imaging applications. Methodologies that help distinguish different tissues, tissue properties, or tracers could help maximize the diagnostic information and guide treatments in a clinical scenario.

Parallel with the technological advancements in medical imaging, several methods were developed to differentiate tissue properties or materials within a body by sensitizing the signals to different physical properties. Localizing different signal responses spatially in a medical imaging scenario effectively leads to color imaging (i.e., quantitative mapping), which enables distinguishing of tissue properties, functional markers, and environmental conditions such as temperature and viscosity within a medium.

1.1 Current Color Medical Imaging Modalities

In MRI, there are several methods for quantitative mapping of different tissues. The mapping of tissue relaxation times T1 and T2 takes advantage of different relaxation mechanisms of the nuclei under a magnetic field and an RF pulse. T1 and T2 are different for different tissue compositions, which enables the main tissue contrast in MRI. T1 and T2 imaging are used together or with other MRI procedures to distinguish different tissues or tissue properties for increased diagnostic capability. Some applications include brain imaging [1], cardiovascular imaging [2, 3], and liver diseases [4]. Additionally, diffusion MRI quantifies the random movement of water molecules in the human body. Different tissues have different cellular structures and hence have characteristic diffusion properties. Diffusion weighted imaging (DWI) provides information about the diffusion properties [5, 6]. Furthermore, axon membranes limit movement of water molecules, and MRI enables imaging of microstructural details in the brain through diffusion tensor imaging (DTI) [7, 8]. DWI and DTI are used in the diagnosis of various white matter diseases such as Alzheimer's disease [9] and stroke [10], as well as various cancers [11, 12]. Functional MRI (fMRI) is another method of mapping depending on the blood oxygenation during electrical activity in the brain. fMRI utilizes a third relaxation mechanism, $T2^*$, which changes during altered brain activity [13]. Applications of fMRI focuses on the brain injuries [14, 15], diseases such as Alzheimer's disease [16] or multiple sclerosis [17], and understanding the functional role of different parts of the brain [18]. Finally, the chemical environments of the materials cause a shift of their respective proton resonance frequencies. Discovery of this property led to the separation of water and fat protons and effectively enabled non-invasive imaging of two different tissues in the same medium [19]. Magnetic resonance spectroscopic imaging (MRSI) is another important MRI technique that relies on detecting the chemical shift among various metabolites within a voxel, with numerous possible applications in cancer and heart disease diagnosis [20, 21, 22, 23] to neuroscience [24, 25]. In addition, several MRI methods, such as perfusion MRI [26] and dual-nuclei MRI [27, 28], use both magnetic and non-magnetic markers as contrast agents.

In CT, differences in the X-ray attenuation rates of different materials enables the ability to differentiate different tissue types or contrast agents, such as iodine-based contrast media or inhaled xenon gas. Although dual-energy CT (DECT) was conceived early on, it was not widely used in clinical scenarios [29, 30]. However, with the recent developments in the CT equipment, there is a renewed interest in DECT [31, 32]. The added functionality of material and tissue differentiation to traditional CT increased its effectiveness for diagnosis and treatment. The applications range from cancer [33, 34, 35] to lung diseases [36], as well as to imaging of cardiovascular [37] and musculoskeletal system [38].

For single-photon emission computerized tomography (SPECT) and positron emission tomography (PET), the simultaneous detection of different tracers based on their different emission energies is utilized to quantize the amount of certain tracers within a medium. Dual isotope SPECT and PET are often used to measure the amount of tracers absorbed by the tissue to assess certain diseases, from cancer to diabetic infections [39, 40]. These dual isotope modes can be further used to colorize the generated image in a wide range of medical applications [41, 42, 40]. SPECT and PET are also used in conjunction with CT to fuse the high sensitive metabolic image provided by SPECT or PET and the anatomic information provided by CT [43].

Similar to SPECT and PET, near-infrared fluorescence imaging (NIRFI) aims to achieve color images via detection of different tracers sensitive to different wavelength photons [44, 45, 46, 43]. In addition, NIRFI can be used in conjunction with PET, utilizing tailored tracers with simultaneous radioactive and fluorescent properties, effectively creating a dual-purpose probe [47, 48]. NIRFI has an active use in clinical applications in both diagnosis and treatment [44, 48], and with real-time color imaging capabilities [45, 49].

Finally, US is also capable of color imaging. Color Doppler imaging (CDI) utilizes the movements inside the medium to detect the flow of materials, mainly the blood inside the arteries and vessels [50, 51]. This technique is based on differentiating the moving parts inside a medium from the stationary tissue, which enables detection of even the smallest blood vessels. It is mainly used for diagnostic purposes to identify and measure the blood flow around a targeted tissue [52, 53, 54, 55].

For CT, SPECT, and PET, the ionizing radiation and radioactive tracers have detrimental effects on the human body, which in turn limit the applicable patient profile and exposure time. However, CT is the only tomographic imaging modality that can generate high-resolution images with very short acquisition times. This property of CT also makes it the state-of-the-art method for most emergency imaging scenarios and cardiovascular interventions, since they require high imaging speed and real-time imaging capability. The utilization of NIRFI in clinical scenarios is restricted due to the toxicity levels of the required contrast agents. Nevertheless, several NIRFI probes and contrast agents are considered to have low toxicity levels [46, 56, 43]. Additionally, NIRFI lacks the depth penetration capability of other imaging techniques [57, 58]. US is cheap, widely available, and safe, but it also lacks the depth penetration capability that is possible by most other medical imaging methods. Additionally, CDI requires moving parts (i.e., blood within the vessels) and stationary tissue around the targeted area to generate color images [51]. This requirement limits the method's applicability, and the quality of the generated image is highly dependent on the attenuation of the clutter signals originating from slowly moving tissue [59, 60]. MRI is a safe medical imaging modality that does not use ionizing radiation or toxic contrast agents, and has good resolution and excellent depth penetration. MRI offers various quantitative imaging opportunities that can differentiate different tissues (T1/T2 weighting), tissue properties (DWI), or contrast agents. The main disadvantage of MRI is that the imaging procedures take several minutes to an hour, which limits the application of MRI methods to non-emergency clinical scenarios. Different imaging modalities can also be combined together, for example, PET-CT [61, 62], PET-MRI [62, 63] or NIRFI-PET [47], to create a composition of anatomical image and quantitative mapping.

1.2 Magnetic Particle Imaging as a Safe and Fast Medical Imaging Modality

Magnetic particle imaging (MPI) is a rapidly developing tracer-based medical imaging modality, which takes advantage of the non-linear response of magnetic nanoparticles (MNPs) under time-varying magnetic fields [64, 65, 66, 67, 68]. The leading applications of MPI include angiography [69, 70], stem cell tracking [71, 72, 73], inflammation imaging [74, 75], drug delivery [76, 77], traumatic brain injury imaging [78], cancer imaging [79], and localized hyperthermia [80].

A standard MPI system utilizes three different magnetic fields to acquire an image of the spatial distribution of MNPs. First, a field free point (FFP) is created using a static selection field (SF) with strong spatial gradients. Then, a sinusoidal drive field (DF) is applied to move the FFP in a field-of-view (FOV). However, human safety concerns [81, 82] and/or hardware limitations constrain the region covered by the DF to a relatively small partial field-of-view (pFOV) around the FFP. Thus, additional low-frequency focus fields (FFs) are employed to shift the FFP in a wider FOV [83].

MPI safety issues are focused on two different topics: (1) the safety of the MNPs that are used as tracers, and (2) the safety of the magnetic fields utilized during imaging. Accumulation and distribution of MNPs are the leading safety concerns for the tracers. The biodistribution of MNPs depends on the particle size, coating, and amount of particles administrated during the imaging procedure. MNPs are typically removed from the bloodstream relatively quickly and are mainly accumulated in the liver and the spleen, where they are decomposed into non-toxic sub-particles [84, 85]. Modifying the MNP structure can further increase biocompatibility by physical means or decrease the toxicity by increasing the received signal intensity (i.e., by reducing the detectable dosage requirements for MNP). Nevertheless, MNP toxicity is an active research topic [84, 86, 85]. In terms of magnetic field safety, peripheral nerve stimulation (PNS) limits and specific absorpiton rate (SAR) tissue heating limits need to be considered [87, 88]. PNS is considered to be the main safety concern for the kHz range magnetic fields used in MPI [87]. PNS is the stimulation of peripheral nerves due to the rapid changes in the magnetic field that causes sensory responses in tissue. It is described as a tingling or poking sensation, and is a limiting factor for the gradient magnetic fields in MRI, as well [89]. Finally, one of the main challenges of MPI is the lack of commercial systems in the human scale. While there are several working systems for small animal imaging, scaling an MPI scanner to human sizes remains a critical challenge.

Despite the aforementioned challenges, MPI features numerous advantages that makes it a highly promising imaging modality. Firstly, MPI offers high sensitivity and high resolution, where the received signal only reflects the MNP concentration without any background signal from the tissue [90]. The duration of the magnetic fields used in MPI are relatively short and the MNPs respond to the magnetic fields near instantaneously, offering a possibility for real-time imaging capability [91, 92, 93, 94]. Furthermore, MPI does not utilize ionizing radiation and commercial MNPs are considered to be highly biocompatible [95]. Finally, there is an active effort to scale MPI scanners to the human size in the research settings [96, 97, 98].

1.3 Quantitative Mapping via Color MPI

Color MPI is an emerging quantitative mapping field within MPI, providing a means to distinguish different MNPs and/or MNP environments [99]. The primary method for color MPI is identifying different MNPs through their responses to changes in the magnetic field. However, the magnetization mechanisms involved with MNPs also provide a means to distinguish the properties of the environments that MNPs reside in, such as their viscosity and temperature. Color MPI offers various practical applications such as catheter tracking during cardiovascular interventions [100, 92], and identifying the characteristics of the environment such as viscosity [101, 102, 103, 104, 105] and temperature [106, 107, 108].

Depending on factors such as the magnetic material and core diameter, different MNPs are expected to have different MPI signal responses [66]. Additionally, differences in the environmental conditions such as temperature or viscosity can alter the relaxation behavior of the MNPs [109]. Recently, color MPI techniques have been proposed to take advantage of these differences to distinguish the MPI signals from different MNPs and/or environmental conditions. The first color MPI study targeted distinguishing MNPs using a system function reconstruction (SFR) approach [99]. SFR requires lengthy calibration measurements of a point source MNP at all voxel locations within a FOV [110, 111]. For the color MPI extension, an extended linear system of equations is solved to find the concentrations of different MNP types and/or MNPs in different environmental conditions for each voxel. SFR-based color MPI requires separate calibrations for each MNP type and/or environmental condition, further lengthening the calibration time [99, 100, 93, 106].

X-space-based color MPI techniques do not require calibration, but the resulting images are typically blurred by the point spread function (PSF) of the imaging system [112]. One approach is performing multiple measurements at different drive field (DF) amplitudes to differentiate the relaxation behaviors of MNPs [113]. Another approach is a relaxation time constant (τ) estimation method, abbreviated as TAURUS (τ estimation via Recovery of Underlying mirror Symmetry) [101, 104, 114]. Instead of estimating the concentrations of different MNPs like the SFR-based color MPI methods, TAURUS estimates a τ for each pFOV (or patch) within the image to create a quantitative τ map. Importantly, it does not require any calibrations, multiple measurements, or prior knowledge about the MNPs to estimate the τ map. However, TAURUS relies on the underlying mirror symmetry of the MPI signal, which is valid only for trajectories that perform a strict back-and-forth scanning of each pFOV (e.g., a 1D DF applied together with constant FFs). This requirement restricts the usage of TAURUS to trajectories with constant or piecewise constant FFs, previously demonstrated for active scan times exceeding 2.5 minutes for a 0.8 cm×8 cm FOV [114]. Reducing the scan time can pave the way to real-time imaging applications of TAURUS [94].

1.4 Motivation

Color MPI offers increased functionality for the diagnosis and treatment of various diseases. For example, color MPI can be a safe alternative to CT for angiography [115], a fast alternative to MRI for brain injury and stroke imaging [116], and a safe alternative for monitoring cancer treatment when used together with magnetic fluid hyperthermia [117].

Current color MPI methods require long calibration scans (i.e., separate scans for each MNP type and/or environmental condition) and have increased computational complexity [99, 100, 106, 93]. On the other hand, calibration-free and computationally simple methods are limited to imaging procedures with long scan times [113, 114].

The primary motivation of this thesis is to provide a calibration-free and computationally efficient method to achieve color MPI for imaging procedures with short scan times to reach real-time scanning capability. Real-time color MPI can provide a means for the diagnosis and treatment monitoring of many critical injuries and diseases such as stroke and cancer. Real-time color MPI can also enable a safe, non-ionizing alternative for interventional imaging and cancer treatment monitoring.

1.5 Outline

This thesis proposes a novel method for achieving color MPI with real-time imaging capabilities for distinguishing different MNPs and/or MNP environments. To achieve rapid, relaxation-based, and calibration-free color MPI, a previously proposed color MPI method abbreviated as TAURUS is extended to fast and multidimensional MPI scanning trajectories. Short scan sequences require time-varying, continuous, and rapid movement of the field-free region (FFR). This movement distorts the primary mechanism involved in TAURUS to estimate the MNP properties, which are exploited in distinguishing the MNP types and MNP environments. This thesis investigates this distortion theoretically and experimentally using extensive simulations and experiments in an in-house MPI system. A novel method for the correction of this distortion is proposed. Importantly, the parameters of the proposed approach depend only on the MPI system properties and are computationally efficient to implement. Additionally, the first simulation work for relaxation-based real-time color MPI is presented based on the proposed method.

The organization of this thesis is as follows:

- In Chapter 2, the theoretical background of MNPs, MPI, and the state-of-the-art image reconstruction methods for MPI are presented. MNP relaxation is a primary mechanism of MNPs that is involved with identifications of both different MNPs and different MNP environments. Relaxation mechanisms and how different image reconstruction methods use this property for color MPI image generation are explained in this chapter. The original TAURUS method is also presented.

- In Chapter 3, the proposed rapid TAURUS method is introduced. First, the distortions caused by the time-varying, continuous, and rapid movement of the FFR on the mirror symmetry of the MPI signal (the primary mechanism involved with TAURUS) is explained. Then, this chapter introduces the theory of the proposed novel method for correcting these distortions. The theory is supported by extensive simulations and MPI experiments for different scanning sequences. Details of the simulations and experiments and the results are presented. Chapter 3 ends with discussions and possible solutions on rapid relaxation-based MPI.

- In Chapter 4, rapid TAURUS for real-time relaxation-based color MPI is presented. The method utilizes rapid TAURUS introduced in detail in Chapter 3. The fast scanning sequences presented in this chapter have scanning times on the order of milliseconds. The simulation parameters and results are explained, and possible improvements are discussed to decrease the scanning time and to increase the quality of the generated color MPI image. Additionally, the computational complexity and processing times of the method are further explained in this chapter.

- The capabilities of rapid TAURUS presented in this thesis to generate color MPI images are summarized in Chapter 5. The potential extensions of the proposed work in this thesis are also briefly discussed as future work.

Chapter 2

Theoretical Background of MPI

2.1 Magnetic Nanoparticles and MPI System Overview

MPI aims to image MNPs introduced into the human body. There are several FDA and EMA approved MNPs with iron oxide cores already used in MRI and their behaviors are well known [118, 119]. MNPs consist of two main parts: the first is the magnetic core that is responsible for magnetization and signal generation, and the second part is a nonmagnetic coating to ensure that the MNPs show superparamagnetic behavior and are biocompatible [120]. Magnetization behavior of MNPs are described by the Langevin theory. On a macroscopic scale, Brownian motion results in the net magnetic moment to be zero in the absence of an external field. When an external magnetic field is applied, it aligns the individual magnetic moments of the MNPs, resulting in a net magnetization. The amount of magnetization does not have a linear relationship with the applied external magnetic field. The magnetization changes rapidly within a narrow region around zero field, and saturates after a certain field amplitude. This magnetization response is illustrated in Fig. 2.1. This saturation response of MNPs as explained by the Langevin theory is pivotal for encoding the received

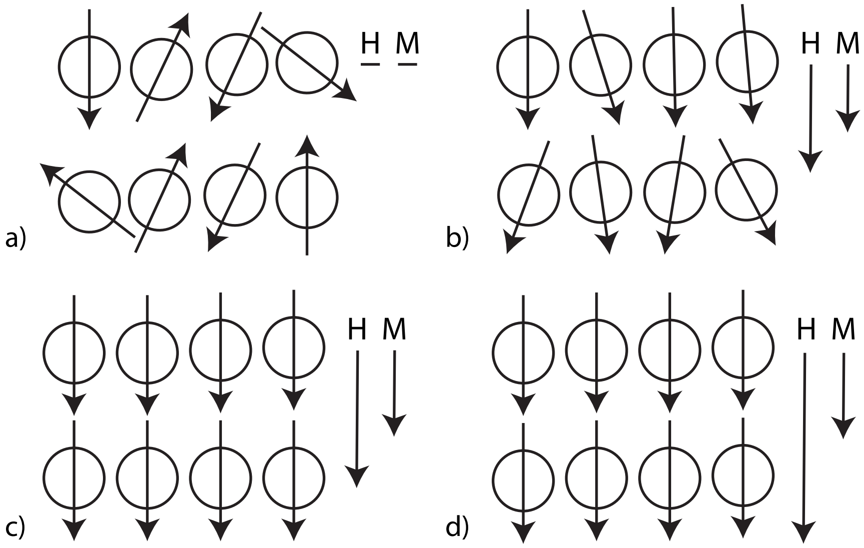

Figure 2.1: Effects of applied external field on the magnetization of an ensemble of MNPs. (a) There is zero net magnetization in the absence of external magnetic field. (b) The magnetization changes rapidly to align with the applied field, and (c-d) reaches saturation as the field is further increased.

signal to a point in space in MPI.

The nonlinear magnetization behavior of the MNPs can be modeled using the Langevin function as follows [112, 121, 120]:

$$M(H) = c\ m\mathcal{L}(kH) = c\ m\left(\coth(kH) - \frac{1}{kH}\right), \tag{2.1}$$

where

$$k = \frac{\mu_0 m}{k_B T}. \tag{2.2}$$

Here, M is the magnetization of MNPs, H is the applied magnetic field, c (particles/m^3) is the MNP concentration, μ_0 is the vacuum permeability, k_B is the Boltzmann constant, T (K) is the temperature, and m is the magnetic moment of a single MNP. For a single domain spherical MNP with diameter d, $m = M_{\text{sat}}\pi d^3/6$, and $M_{sat} = 0.6$ T$/\mu_0$ for magnetite MNPs [112].

Figure 2.2 depicts the Langevin function and its derivative. After the applied magnetic field exceeds the narrow non-linear region around $H = 0$, the MNPs get saturated and can no longer react to the external applied magnetic field. This

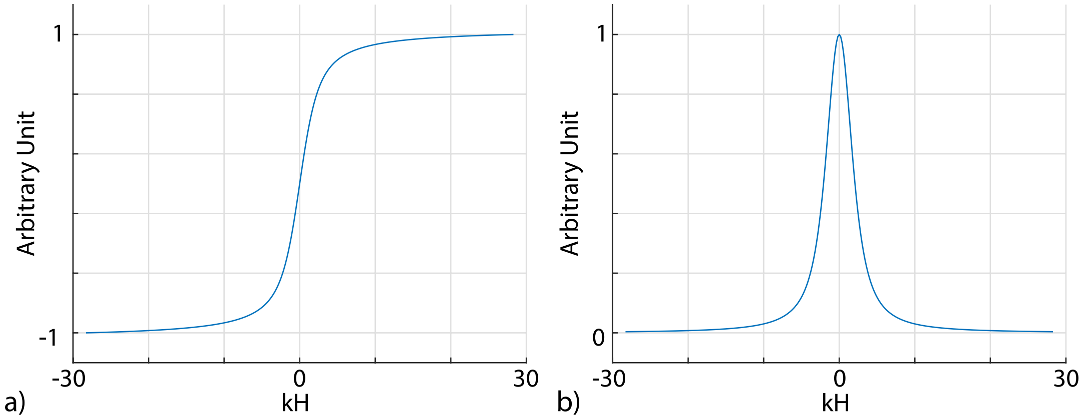

Figure 2.2: (a) Langevin function as given in Eq. (2.1) and (b) its derivative. In MPI, the magnetization response is recorded using an inductive receive coil, which results in a signal that is described by the derivative of the Langevin function.

non-linear magnetization response is utilized to create spatial encoding inside an MPI system. The field-of-view (FOV) is magnetically saturated except a field-free-region (FFR) at the center of the MPI system, using magnets. This saturation generating field is called the selection field (SF). If the FOV is excited using an additional time-varying magnetic field called the drive field (DF), only the MNPs that are spatially within/near the FFR will be able to react. This configuration of magnetic fields creates spatial encoding in MPI. Then, the time-varying magnetization of the MNPs within/near the FFR induces a signal in an inductive receive coil. Figure 2.3.(a) shows a conventional MPI system with permanent magnets creating the SF, together with the DF coil and the receive coil placed around the FFR. Figure 2.3.(b) shows the combined effects of the SF and DF on the Langevin function and the received signal in different regions within the FOV.

In Figure 2.3, when the FFR is in the shape of a point, it is called a field free point (FFP). Then, the sinusoidal DF is applied to move the FFP in the FOV. However, human safety concerns [81, 82] and/or hardware limitations constrain the region covered by the DF to a relatively small partial field-of-view (pFOV) around the FFP. Thus, additional low-frequency fields called focus fields (FFs) are employed to shift the FFP in a wider FOV [83]. The MNP responses are picked up using a receiver coil using the reciprocity principle. The generated

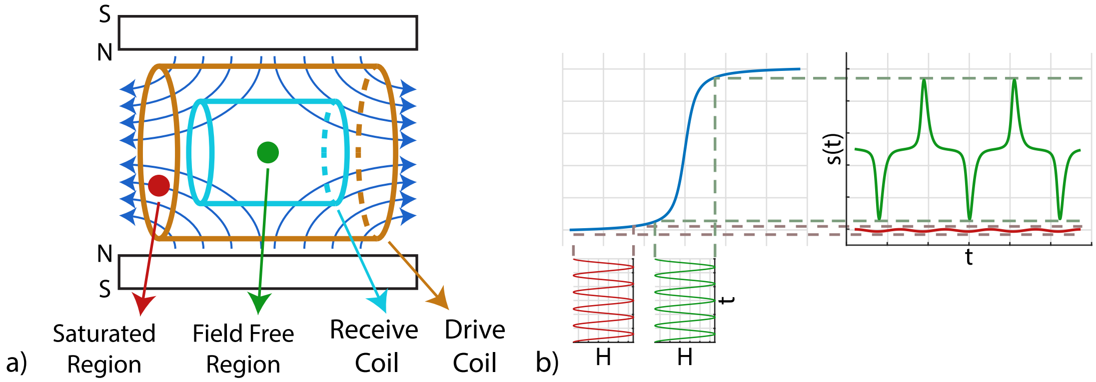

Figure 2.3: (a) Topology of a conventional MPI system with permanent magnets creating the FFR and the saturated regions. Drive and receive coils are placed around the FFR. (b) An applied magnetic field generates minimal response around the saturated region and generates substantial response around the FFR, resulting in spatial encoding.

signal is then turned into an MPI image using image reconstruction technqiues, such as system function reconstruction (SFR) or x-space reconstruction.

2.2 MPI Signal and Image Reconstruction Methods

There are two commonly employed methods for image reconstruction in MPI. SFR depends on calibration scans encapsulating the MNP responses in different spatial locations for image reconstruction. X-space based image reconstruction utilizes an analytical MPI signal equation, and grids the signal to the instantaneous location of the FFP to form the image. These image reconstruction methods are briefly explained below.

2.2.1 System Function Reconstruction

The SFR method takes advantage of the idea that the MPI signal can be expressed as a linear combination of signals from independent particle distributions within a FOV. In SFR, first a system matrix is collected by placing a point source MNP distribution within each voxel position inside the FOV. A calibration scan for any type of FFP trajectory is utilized to collect a calibration signal for that voxel position, and the Fourier transform of the recorded signal is placed at the corresponding column of the system matrix, **S**. This process is illustrated in Figure 2.4 and is repeated for each voxel position to build the system matrix.

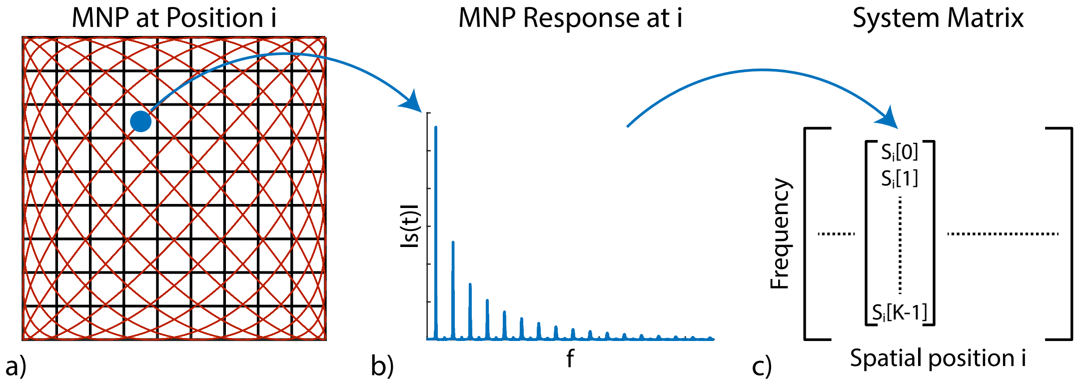

Figure 2.4: (a) A point source particle is placed in the i^{th} voxel and the imaging sequence is applied, (b) Fourier transform of the received signal is computed, and (c) placed into the i^{th} column of the system matrix, **S**.

Once the system matrix is collected, the imaging process can begin. During the imaging experiment, the signal response from MNP distribution of interest (e.g., MNPs within the blood vessels) are acquired. Then, the MNP concentrations at all voxel positions can be calculated via solving a linear system of equations,

$$\mathbf{S}\mathbf{c} = \mathbf{u}, \tag{2.3}$$

where **u** is the Fourier transform of the received signal during imaging. In addition, **c** is the vector of MNP concentrations at voxel positions within the FOV, which corresponds to the vectorized version of the desired MPI image. The advantage of the SFR method is that it accounts for all possible influences of the environment, including the system non-idealities. Therefore it has robustness against numerous system imperfections such as SF and DF inhomogeneities and results in good spatial resolution.

The SFR method is easy to deploy and results in high-quality reconstructions. However, calibration scans require sensitive positioning of the point source MNP, which is typically achieved by high-accuracy robotic actuators. Due to the mechanic movement of the actuators, the calibration becomes a lengthy procedure [110, 111]. There are several methods proposed to decrease the calibration time with resolution trade-offs [122, 123, 124, 125]. Additionally, solving the inverse problem in Eq. (2.3) requires several seconds to minutes, depending on the desired image quality. In a real-time imaging scenario, this relatively high computation time negates the primary advantage of MPI, which is fast signal encoding. However, real-time image reconstruction is a desired property for direct feedback in several applications, such as vascular interventions.

2.2.2 X-space MPI

Compared to the SFR based methods, x-space reconstruction offers a fast and direct reconstruction of the MPI image. The x-space reconstruction utilizes the idea of spatial encoding, together with the Langevin response of the MNPs given in Eq. (2.1). Under a time-varying DF, $H_0(t)$, and a position-dependent SF, $H_S(x)$, the total magnetic field can be written as [112, 121, 120]:

$$H(x,t) = H_0(t) + H_S(x), \tag{2.4}$$

where

$$H_S(x) = -Gx, \tag{2.5}$$

Here, $H(x,t)$ is the position- and time-dependent total magnetic field. The SF is assumed to change linearly as a function of position, with a gradient of $-G$ (the negative sign is introduced for convenience). Solving for $H(x,t) = 0$ yields the instantaneous position of the FFP:

$$x_s(t) = \frac{H_0(t)}{G}. \tag{2.6}$$

Then, the superposition of the DF and SF can be expressed in terms of the FFP position as follows:

$$H(x,t) = G(x_s(t) - x). \tag{2.7}$$

The magnetization of MNPs were described by the Langevin function in Eq. (2.1), which is dependent on the external field $H(x,t)$. Then, combining Eq. (2.1) and

Eq. (2.7), the time-varying magnetization for a 1D MNP distribution $c(x)$ can be written as:

$$M(x,t) = c(x)m\mathcal{L}\big(kG(x_s(t) - x)\big). \tag{2.8}$$

Since the magnetization is time varying, it will generate an electrical voltage in an inductive coil. Therefore, a receive coil is utilized to collect the magnetization response of MNPs. The received signal can be written as the volume integral of the time derivative of the magnetization as follows:

$$\begin{aligned} s_{adiab}(t) &= -\mu_0 B \int \frac{\partial M(u,t)}{\partial t} dV \\ &= -\mu_0 Bm \int\int\int c(u)\delta(v)\delta(w) \frac{\partial \mathcal{L}\big(kG(x_s(t) - u)\big)}{\partial t} dudvdw. \end{aligned} \tag{2.9}$$

Here, B is the sensitivity of the inductive receiver coil. Using the chain rule, the 1D adiabatic MPI signal (i.e., the MPI signal under the assumption of instantaneous MNP alignment, without relaxation) can be written as [112]:

$$s_{\text{adiab}}(t) = Bmc(x) * \dot{\mathcal{L}}\big(kGx\big)\Big|_{x=x_s(t)} kG\dot{x}_s(t), \tag{2.10}$$

Here, $*$ denotes convolution over x, $\dot{\mathcal{L}}$ is the derivative of the Langevin function and is well behaved as shown in Fig. 2.2, and $\dot{x}_s(t)$ is the time derivative of the FFP position (i.e., the instantaneous FFP speed). Note that the spatial encoding of the MPI signal $s(t)$ is evident in Eq. (2.10).

Once $s(t)$ is gathered, the x-space MPI image can be reconstructed using the following relation:

$$IMG(x_s(t)) = \frac{s_{\text{adiab}}(t)}{BmkG\ \dot{x}_s(t)} = c(x) * h(x)\Big|_{x=x_s(t)}, \tag{2.11}$$

where

$$h(x) = \dot{\mathcal{L}}\big(kGx\big). \tag{2.12}$$

Accordingly, the MPI image is reconstructed by speed-compensating the received signal, and assigning it to the instantaneous FFP position. The resulting MPI image is the particle distribution blurred by $h(x)$, the point spread function (PSF). Here, the PSF corresponds to derivative of the Langevin function, and is a function of both the MNP parameter k and the MPI system parameter G.

Extension of the 1D x-space model to multidimensional FFP trajectories was further explored in the literature, showing that x-space MPI is a powerful technique for fast image reconstruction [121]. X-space MPI image reconstruction does not require any calibration scans, but the PSF of the imaging system typically blurs the resulting images as illustrated in Figure 2.5. The original x-space method was proposed for piecewise FFs in which the FFP was moved to a constant position, and a sinusoidal DF was used to excite the MNPs. This process was repeated at many positions to densely cover the FOV. Consequently, trajectories with piecewise FFs slow down the scanning process and restrict the potential computational speed of the reconstruction. Several other methods were proposed to extend the x-space reconstruction to more complex and faster trajectories [126, 127].

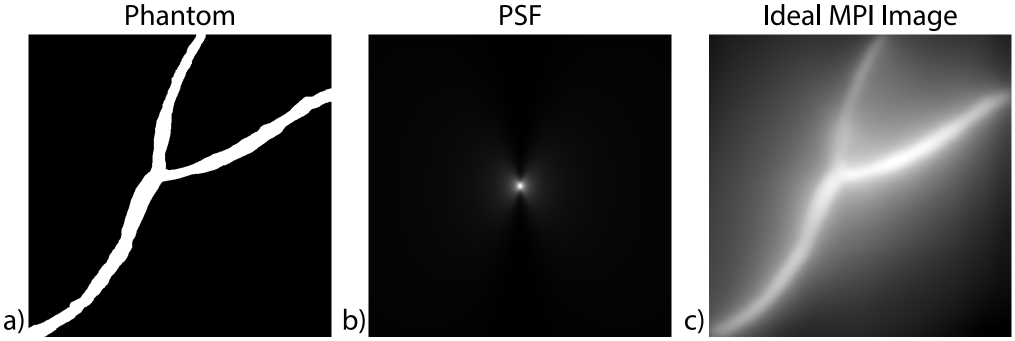

Figure 2.5: Ideal x-space MPI image as a result of blurring of phantom by the PSF. (a) 7×7 cm^2 vasculature phantom used in the simulation, (b) PSF of the MPI system for a MNP with 25 nm diameter and an MPI system with (-4.8, 2.4, 2.4) T/m SF gradients in the x-, y- and z-directions, and (c) the resulting ideal x-space MPI image.

2.3 Effects of Relaxation on the MPI Signal

The MPI signal in Eq. (2.10) is the adiabatic signal, which assumes that the particles instantly align with the changing magnetic field. In practice, the alignment of the particles lag due to the relaxation phenomenon. There are two main relaxation processes: 1) Néel relaxation due to the rotation of the magnetization vector of the particle, and 2) Brownian relaxation due to the physical rotation of the particle. The Néel and Brownian rotations are illustrated in Figure 2.6.(a). These relaxation processes are associated with relaxation time constants as follows [128, 129]:

$$\tau_N = \tau_0 \frac{\sqrt{\pi} e^{\sigma}}{2\sqrt{\sigma}}, \tag{2.13a}$$

$$\tau_B = \frac{3\nu V_h}{k_B T}, \tag{2.13b}$$

where

$$\sigma = \frac{K V_c}{k_B T} \tag{2.14}$$

In Eq. (2.13a), τ_0 is the attempt time [129], K is the anisotropy constant of the MNPs, and σ is the ratio of anisotropic and thermal energies of the MNP. In Eq. (2.13b), ν is the viscosity of the environment, and V_h is the hydrodynamic volume of the MNPs.

It was suggested that the Néel and Brownian relaxation mechanisms work in parallel, resulting in a net effective time constant of [129]:

$$\tau_{eff} = \left(\frac{1}{\tau_N} + \frac{1}{\tau_B} \right)^{-1}. \tag{2.15}$$

However, these two relaxation mechanisms describe the motion of MNPs under zero-field conditions (i.e., when the applied field is removed). In contrast, there are several superimposed and time-varying magnetic fields in MPI. Hence the relaxation mechanism in MPI shows different properties than the Néel and Brownian relations given above [128].

In MPI, a simplifying approach is to model the relaxation effect as a Debye process, which can be expressed as a convolution relation [109]:

$$s(t) = s_{\text{adiab}}(t) * r_\tau(t), \tag{2.16a}$$

$$r_\tau(t) = \frac{1}{\tau} e^{-t/\tau} u(t). \tag{2.16b}$$

Here, $*$ denotes convolution over t, $s(t)$ is the signal with relaxation, $s_{\text{adiab}}(t)$ is the adiabatic signal described by the Langevin model in Eq. (2.10), and $r_\tau(t)$ is the relaxation kernel. In the relaxation kernel, τ (sec) is the effective relaxation

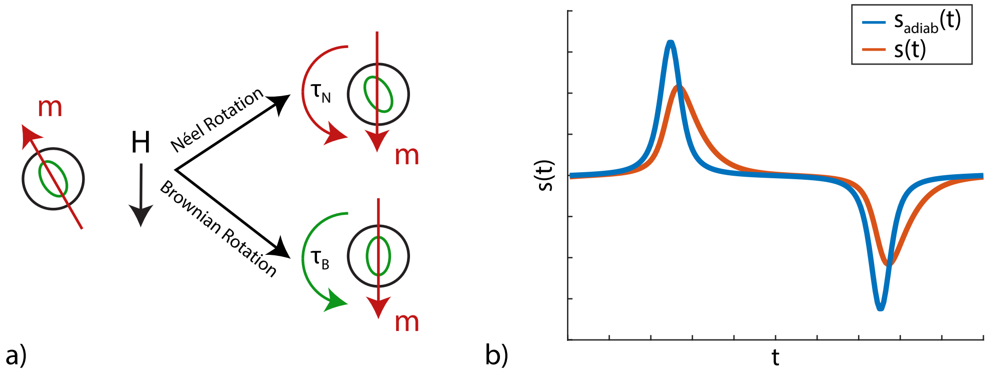

Figure 2.6: Relaxation and its effects on the MNP and MPI signal. The MNP is illustrated with its magnetic moment (red arrow), magnetic core (green ellipse) and coating around the core (black circle). (a) The Néel relaxation internally rotates the magnetic moment and the Brownian relaxation externally rotates the entire MNP. (b) The effects of the MNP relaxation on the MPI signal. The signal with relaxation, $s(t)$, is delayed and has reduced amplitude when compared to the adiabatic signal, $s_{\text{adiab}}(t)$.

time constant of the MNP that explains the signal lag and $u(t)$ is the Heaviside unit step function [109]. The relaxation in this sense creates an additional layer of blurring and lowers the amplitude of the adiabatic MPI signal as shown in Figure 2.6(b).

2.4 Distinguishing MNP Responses via Color MPI

Depending on factors such as the magnetic material and core diameter, different MNPs are expected to have different MPI signal responses [66]. Additionally, differences in the environmental conditions such as temperature or viscosity can alter the relaxation behavior of the MNPs [109]. Color MPI techniques aim to take advantage of these differences to distinguish the MPI signals from different MNPs and/or environmental conditions.

2.4.1 SFR-based Color MPI

SFR accounts for all possible influences of the environment and MNPs, including the abovementioned relaxation properties. Accordingly, the first color MPI study targeted distinguishing MNPs using the SFR approach [99]. For the color MPI extension, an extended linear system of equations is solved to find the concentrations of different MNP types and/or MNPs in different environmental conditions for each voxel. The extended linear system of equations is expressed as follows:

$$\mathbf{S_1 c_1} + \mathbf{S_2 c_2} + ... + \mathbf{S_n c_n} = \mathbf{u}, \tag{2.17}$$

where $\mathbf{S_j}$ are different system matrices for different MNP types and/or environmental conditions, $\mathbf{u}$ is the Fourier transform of the received signal during imaging, and $\mathbf{c_j}$ are the concentrations of different MNP types and/or MNPs in different environmental conditions in the respective voxels. As seen in this equation, SFR-based color MPI requires a separate calibration scan to determine the system matrix $\mathbf{S_j}$ for each MNP type and/or environmental condition. This process further lengthens the calibration time, as well as increasing the computational cost of the problem [99, 100, 106, 93].

2.4.2 TAURUS - TAU estimation via Recovery of Underlying mirror Symmetry

Several color MPI methods that exploit the x-space signal definition were proposed. One approach is performing multiple measurements at different drive field (DF) amplitudes to differentiate the relaxation behaviors of MNPs [113]. Another approach is a relaxation time constant (τ) estimation method, abbreviated as TAURUS (τ estimation via Recovery of Underlying mirror Symmetry) [101, 104, 114]. Instead of estimating the concentrations of different MNPs and/or environmental conditions like the SFR-based color MPI methods, TAURUS estimates a τ for each pFOV (or patch) within the image to create a quantitative τ map. Importantly, it does not require any calibrations, multiple measurements, or prior knowledge about the MNPs to estimate the τ map. However, TAURUS relies on the underlying mirror symmetry of the MPI signal, which is valid only for trajectories that perform a strict back-and-forth scanning of each pFOV (e.g., a 1D DF applied together with constant FFs). This requirement restricts the usage of TAURUS to trajectories with constant or piecewise constant FFs, previously demonstrated for active scan times exceeding 2.5 minutes for a 0.8 cm×8 cm FOV [114]. Accordingly, the original TAURUS method is computationally fast but was limited by the scanning process. Reducing the scan time can pave the way to real-time imaging applications of TAURUS [94].

Recall that, in MPI, the relaxation effect can be modeled as a Debye process, which can be expressed as a convolution relation as seen in Eqn. 2.16a. TAURUS uses the underlying mirror symmetry of the adiabatic MPI signal to estimate the time constant τ [101, 114]. The mirror symmetry assumption is valid independent of the MNP type or distribution in space, as long as the signal is acquired during a back-and-forth FFP trajectory. Without loss of generality, consider the following trajectory with a 1D DF in the z-direction together with constant FFs:

$$\boldsymbol{x}_s(t) = \begin{bmatrix} x(t) \\ y(t) \\ z(t) \end{bmatrix} = \underbrace{\begin{bmatrix} B_{F,x}/G_x \\ B_{F,y}/G_y \\ B_{F,z}/G_z \end{bmatrix}}_{\text{Focus Field}} + \underbrace{\begin{bmatrix} 0 \\ 0 \\ \frac{B_p}{G_z} cos(2\pi f_d t) \end{bmatrix}}_{\text{Drive Field}}. \tag{2.18}$$

Here, $B_{F,i}$ (T) are the constant FFs and G_i (T/m) are the SF gradients along each direction, respectively. In addition, B_p (T) and f_d (Hz) are the peak amplitude and the frequency of the DF, respectively. The size of pFOV covered by the DF alone is equal to $W_p = 2B_p/G_z$ [66]. This trajectory is referred to as the "piecewise trajectory" (PWT), as it utilizes piecewise constant FFs to scan a small pFOV. Then, $B_{F,i}$ are stepped to different values to cover the entire FOV piece by piece.

For PWT, the negative and positive signals are defined as the half-cycle signals acquired during the back and forth portions of the FFP movement, respectively. Then, the mirror symmetry in $s_{\text{adiab}}(t)$ can be expressed as [101, 114]:

$$s_{\text{pos,adiab}}(t) = -s_{\text{neg,adiab}}(-t) = s_{\text{half}}(t). \tag{2.19}$$

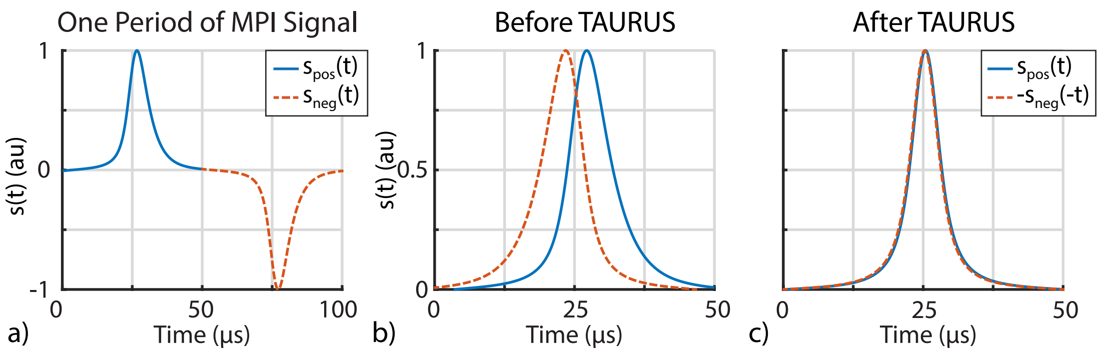

Figure 2.7: Recovery of symmetry via TAURUS. (a) One period of the MPI signal. (b) Shows the broken mirror symmetry before TAURUS and (c) shows the recovered mirror symmetry after TAURUS with $\hat{\tau} = 2.91$ μs. Simulations utilized a point source MNP with $\tau = 3$ μs positioned at $z = 0$.

For the signal with relaxation, however, this mirror symmetry is broken. Using Eqs. (2.16a) and (2.19), can be written as:

$$s_{\text{pos}}(t) = s_{\text{half}}(t) * r_\tau(t) \tag{2.20a}$$

$$s_{\text{neg}}(t) = -s_{\text{half}}(-t) * r_\tau(t). \tag{2.20b}$$

The Fourier transforms of these signals and $r_\tau(t)$ are:

$$S_{\text{pos}}(f) = \mathcal{F}\{s_{\text{pos}}(t)\} = S_{\text{half}}(f) R_\tau(f), \tag{2.21a}$$

$$S_{\text{neg}}(f) = \mathcal{F}\{s_{\text{neg}}(t)\} = -S^*_{\text{half}}(f) R_\tau(f), \tag{2.21b}$$

$$R_\tau(f) = \mathcal{F}\{r_\tau(t)\} = \frac{1}{1 + i2\pi f\tau}. \tag{2.21c}$$

Here, $\mathcal{F}$ denotes Fourier transformation and superscript $*$ denotes complex conjugation. Next, τ can be computed in frequency domain as follows [101, 114]:

$$\tau(f) = \frac{S^*_{\text{pos}}(f) + S_{\text{neg}}(f)}{i2\pi f\left(S^*_{\text{pos}}(f) - S_{\text{neg}}(f)\right)}. \tag{2.22}$$

In Fig. 2.7.(a), one period of the non-adiabatic MPI signal is shown for $\tau = 3$ μs. In Fig. 2.7.(b), positive and mirroded negative non-adiabatic MPI signals show the broken mirror symmetry.

Ideally, $\tau(f)$ should be independent of frequency, f. However, the presence of noise or deviations from the model in Eq. (2.16a) can cause frequency dependency.

To provide robustnesss against such non-idealities, a weighted average of $\tau(f)$ is computed using the magnitude spectrum $|S_{\text{pos}}(f)|$ as weights [114], i.e.,

$$\tau = \frac{\int_0^{f_{\max}} \left|S_{\text{pos}}(f)\right| \tau(f) df}{\int_0^{f_{\max}} \left|S_{\text{pos}}(f)\right| df}. \tag{2.23}$$

Here, For the signal in Fig. 2.7.(b), TAURUS estimates τ as 2.91 μs. Once τ is computed, the mirror symmetric $s_{\text{adiab}}(t)$ can be recovered by deconvolving $s(t)$ with $r_\tau(t)$. After deconvolution the mirror symmetry is recovered, as shown in Fig. 2.7.(c).

Chapter 3

Rapid TAURUS for Relaxation-Based Color Magnetic Particle Imaging

This chapter is based on the following publication:

- M.T. Arslan, A. A. Özaslan, S. Kurt, Y. Muslu and E. U. Saritas, "Rapid TAURUS for Relaxation-Based Color Magnetic Particle Imaging," in IEEE Transactions on Medical Imaging, 2022, DOI: 10.1109/TMI.2022.3195694.

3.1 Introduction

In this chapter, a novel technique that enables τ map estimation via TAURUS for rapid and multi-dimensional trajectories that can reduce the scan time by orders of magnitude is proposed. First, how the time-varying FFs utilized in these trajectories distort the mirror symmetry of the MPI signal is described and a method to compensate for the FF-induced distortions is proposed. Additionally, the performance of TAURUS is improved by casting it as a weighted least squares (WLS-TAURUS) problem. With simulations and imaging experiments, it is demonstrated that the proposed method is robust for a wide range of FF slew rates (SRs) and noise, successfully estimating τ maps for rapid multi-dimensional trajectories while preserving the calibration-free property of TAURUS. The proposed method provides high fidelity τ maps and orders of magnitude reduction in scanning time for TAURUS, demonstrated for over 300-fold reduction in simulations and over 8-fold reduction in experiments.

3.2 Time-varying FF-Induced Distortions

Trajectories that contain time-varying FFs experience a distortion in mirror symmetry, even for the case of $s_{\text{adiab}}(t)$. Without loss of generality, consider the following FFP trajectory, with a 1D DF and a linearly ramping FF applied along the z-direction, and constant FFs in the x- and y-directions:

$$\boldsymbol{x}_s(t) = \begin{bmatrix} x(t) \\ y(t) \\ z(t) \end{bmatrix} = \begin{bmatrix} {}^{B_{F,x}}\!/_{G_x} \\ {}^{B_{F,y}}\!/_{G_y} \\ {}^{R_{s,z}t}\!/_{G_z} \end{bmatrix} + \begin{bmatrix} 0 \\ 0 \\ \frac{B_p}{G_z} cos(2\pi f_d t) \end{bmatrix}. \tag{3.1}$$

Here, $R_{s,z}$ (T/s) is the SR of the FF along the z-direction. As shown in Fig. 3.1, the positive and negative signals have matching amplitudes for $R_{s,z} = 0$. For $R_{s,z} = 20$ T/s, on the other hand, the amplitude is time varying due to the global FFP movement caused by the FF. The pFOV center moves by $R_{s,z}/(2 f_d G_z)$ in half a DF period, so the FFP motion is no longer symmetrical around the pFOV center. In addition, the trajectory speed is different for the positive and negative signals, which further distorts the mirror symmetry in $s_{\text{adiab}}(t)$.

In Fig. 3.2.(a), the positive and mirrored negative signals for $s_{\text{adiab}}(t)$ (i.e., for $\tau = 0$) are plotted, showing the FF-induced distortions on mirror symmetry. The SR along the z-axis causes a lag between these two signals and a mismatch between their amplitudes.

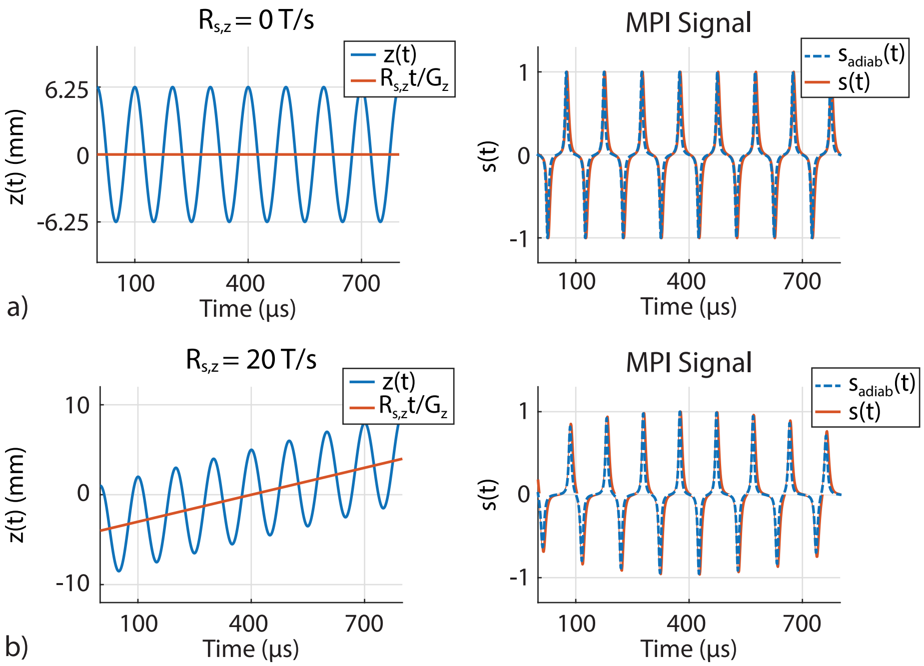

Figure 3.1: Effects of a linearly ramping FF, demonstrating a time-varying signal amplitude at non-zero $R_{s,z}$. The FFP position, and the adiabatic and non-adiabatic signals for (a) $R_{s,z} = 0$ and (b) $R_{s,z} = 20$ T/s. Simulations utilized a point source MNP with $\tau = 3$ μs positioned at $z = 0$.

3.2.1 SR Correction for Recovering FF-Induced Distortions

For accurate τ estimations, an SR correction method is proposed to correct the FF-induced distortions and recover the mirror symmetry in $s_{\text{adiab}}(t)$. First, the FFP speed is assumed to be dominated by the DF for the majority of the FFP motion. For Eq. (4.1), this assumption can be expressed as:

$$\max\left\{\left|\frac{d}{dt}\left(\frac{B_p}{G_z}cos(2\pi f_d t)\right)\right|\right\} \gg \left|\frac{d}{dt}\left(\frac{R_{s,z}}{G_z}t\right)\right|, \tag{3.2a}$$

$$B_p 2\pi f_d \gg R_{s,z}. \tag{3.2b}$$

Here, $\gg$ indicates at least an order of magnitude difference between the left- and right-hand sides of the inequality. Under this assumption, the overall effect of the FF can be approximated as a global time shift and a global amplitude scaling between the positive and negative signals.

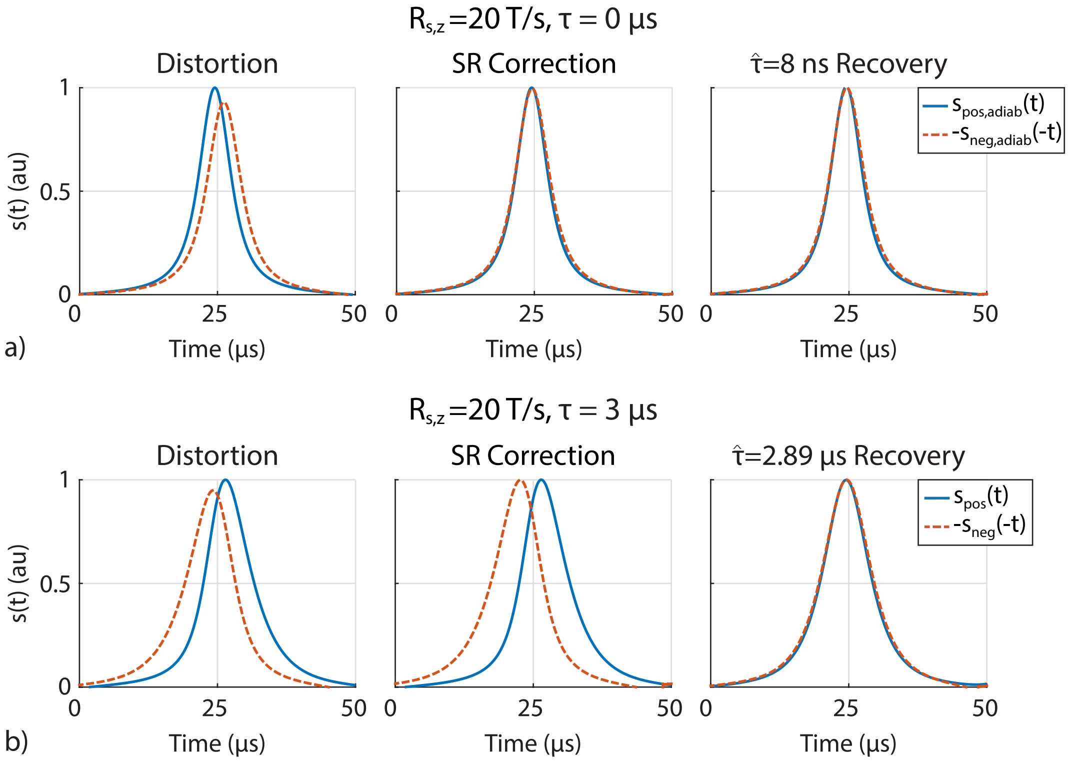

Figure 3.2: FF-induced distortions on mirror symmetry at $R_{s,z} = 20$ T/s for (a) the adiabatic (i.e., $\tau = 0$) and (b) the non-adiabatic (for $\tau = 3$ μs) signals. After SR correction, the mirror symmetry is recovered for the adiabatic signal. After SR correction, TAURUS yields (a) $\hat{\tau} = 8$ ns and (b) $\hat{\tau} = 2.89$ μs.

A closed-form expression for the FF-induced time shift, Δt, can be found by solving the following equation:

$$z(t_0) = z(t_0 + T/2 + \Delta t), \tag{3.3a}$$

$$t_0 = \underset{t}{\operatorname{argmax}}(|\dot{z}(t)|), \quad t \in [0, T/2]. \tag{3.3b}$$

Here, $T = 1/f_d$ is the period of the drive field and t_0 is the time point during the first negative half-cycle at which the FFP speed is maximum. Without loss of generality, consider the trajectory in Eq. (4.1), where t_0 can be found as $1/(4f_d)$. For the same trajectory, Eq. (3.3a) can be expressed as:

$$\begin{aligned} \frac{R_{s,z}t_0}{G_z} + \frac{B_p cos(2\pi f_d t_0)}{G_z} = &\frac{R_{s,z}(t_0 + T/2 + \Delta t)}{G_z} \\ &+ \frac{B_p cos(2\pi f_d(t_0 + T/2 + \Delta t))}{G_z}. \end{aligned} \tag{3.4}$$

Inserting $t_0 = 1/(4f_d)$ gives:

$$B_p cos\left(\frac{\pi}{2}\right) = \frac{R_{s,z}}{2f_d} + R_{s,z}\Delta t + B_p cos\left(\frac{3\pi}{2} + 2\pi f_d \Delta t\right), \tag{3.5}$$

which can be simplified to:

$$B_p sin(2\pi f_d \Delta t) + R_{s,z}\Delta t + \frac{R_{s,z}}{2f_d} = 0. \tag{3.6}$$

If $\Delta t \ll 1/f_d$, a first-order Taylor series expansion of sine yields:

$$\Delta t = \frac{-R_{s,z}}{2f_d(B_p 2\pi f_d + R_{s,z})}. \tag{3.7}$$

A more accurate solution can be computed, e.g., using a higher-order Taylor series expansion of sine.

Next, the amplitude scaling, α, can be expressed as the ratio of the FFP speeds at t_0 and $t_0 + T/2 + \Delta t$, which yields:

$$\alpha = \frac{|B_p 2\pi f_d cos(2\pi f_d \Delta t) + R_{s,z}|}{|-B_p 2\pi f_d + R_{s,z}|}. \tag{3.8}$$

Once Δt and α are computed using Eqs. (3.6)-(3.8), the positive signal can be kept the same and the proposed SR correction can be applied to the negative signal only, i.e.,

$$S_{\mathrm{pos,c}}(f) = S_{\mathrm{pos,d}}(f), \tag{3.9a}$$

$$S_{\mathrm{neg,c}}(f) = S_{\mathrm{neg,d}}(f) e^{i2\pi\Delta t f}\alpha. \tag{3.9b}$$

Here, $S_{\mathrm{pos,d}}(f)$ and $S_{\mathrm{neg,d}}(f)$ are the SR-distorted negative and positive signals, respectively, and $S_{\mathrm{pos,c}}(f)$ and $S_{\mathrm{neg,c}}(f)$ are their corrected versions. Finally, Eq. (2.22) can be applied on the corrected signals to obtain SR-corrected estimation in frequency domain:

$$\tau(f) = \frac{S^*_{\mathrm{pos,c}}(f) + S_{\mathrm{neg,c}}(f)}{i2\pi f\big(S^*_{\mathrm{pos,c}}(f) - S_{\mathrm{neg,c}}(f)\big)}. \tag{3.10}$$

TAURUS was originally proposed for the case of PWT, for which $R_{s,z} = 0$ and Eqs. (3.6)-(3.8) yield $\Delta t = 0$ and $\alpha = 1$, as expected. As $R_{s,z}$ increases, both

Δt and α increase steadily. Importantly, both Δt and α are independent of the MNP parameters or the environmental conditions, and are purely dependent on the system and trajectory parameters.

Estimating τ without applying any SR correction would yield erroneous results. If it is assumed that the SR correction fully recovers the mirror symmetry property, the SR-corrected signals should satisfy Eq. (2.21), i.e.,

$$S_{\mathrm{pos,c}}(f) = S_{\mathrm{half}}(f) R_{\tau}(f), \tag{3.11a}$$

$$S_{\mathrm{neg,c}}(f) = -S^{*}_{\mathrm{half}}(f) R_{\tau}(f). \tag{3.11b}$$

The non-corrected estimation can be expressed by applying Eq. (2.22) directly on the SR-distorted signal, i.e.,

$$\tau_d(f) = \frac{S^{*}_{\mathrm{pos,d}}(f) + S_{\mathrm{neg,d}}(f)}{i2\pi f\big(S^{*}_{\mathrm{pos,d}}(f) - S_{\mathrm{neg,d}}(f)\big)} \tag{3.12}$$

Using Eq. (3.9) and Eq. (3.11), $\tau_d(f)$ can be rewritten as follows:

$$\begin{aligned}\tau_d(f) &= \frac{S^{*}_{\mathrm{pos,c}}(f) + S_{\mathrm{neg,c}}(f) e^{-i2\pi\Delta t f}/\alpha}{i2\pi f\big(S^{*}_{\mathrm{pos,c}}(f) - S_{\mathrm{neg,c}}(f) e^{-i2\pi\Delta t f}/\alpha\big)} &&(3.13\mathrm{a})\\ &= \frac{R^{*}(f)\alpha - R(f)e^{-i2\pi\Delta t f}}{i2\pi f\big(R^{*}(f)\alpha + R(f)e^{-i2\pi\Delta t f}\big)}. &&(3.13\mathrm{b})\end{aligned}$$

Inserting $R(f)$ as given in Eq. (2.21) and simplifying yields:

$$\tau_d(f) = \frac{\alpha(1+i2\pi f\tau) - e^{-i2\pi\Delta t f}(1-i2\pi f\tau)}{i2\pi f\big(\alpha(1+i2\pi f\tau) + e^{-i2\pi\Delta t f}(1-i2\pi f\tau)\big)}. \tag{3.14}$$

The estimation in frequency domain for the SR-distorted case, $\tau_d(f)$, can be expressed as follows:

$$\tau_d(f) = \frac{i2\pi f\tau d_{+} + d_{-}}{i2\pi f\big(i2\pi f\tau d_{-} + d_{+}\big)}, \tag{3.15}$$

where $d_{\pm} = \alpha \pm e^{-i2\pi\Delta t f}$. In the absence of FF-induced distortions (i.e., $R_{s,z} = 0$), $d_{+} = 2$ and $d_{-} = 0$, yielding $\tau_d = \tau$, as expected. However, for increasing FF-induced distortions, τ_d diverges from τ.

In Fig. 3.2, the positive and negative signals of $s_{\mathrm{adiab}}(t)$ (i.e., $\tau = 0$) and $s(t)$ (for $\tau = 3$ μs) are shown for $R_{s,z} = 20$ T/s. For accurate τ estimations,

$s_{\text{adiab}}(t)$ should have a perfect mirror symmetry. However, due to the FF-induced distortions, the positive and the mirrored negative signals of $s_{\text{adiab}}(t)$ are shifted in opposite directions in time in Fig. 3.2.(a). Additionally, the amplitude of the negative signal is smaller than that of the positive signal. When SR correction is applied using Eq. (3.9), the mirror symmetry is recovered for $s_{\text{adiab}}(t)$. Computing τ using TAURUS yields $\hat{\tau} = 8$ ns in this case (i.e., within numerical error of zero, as expected).

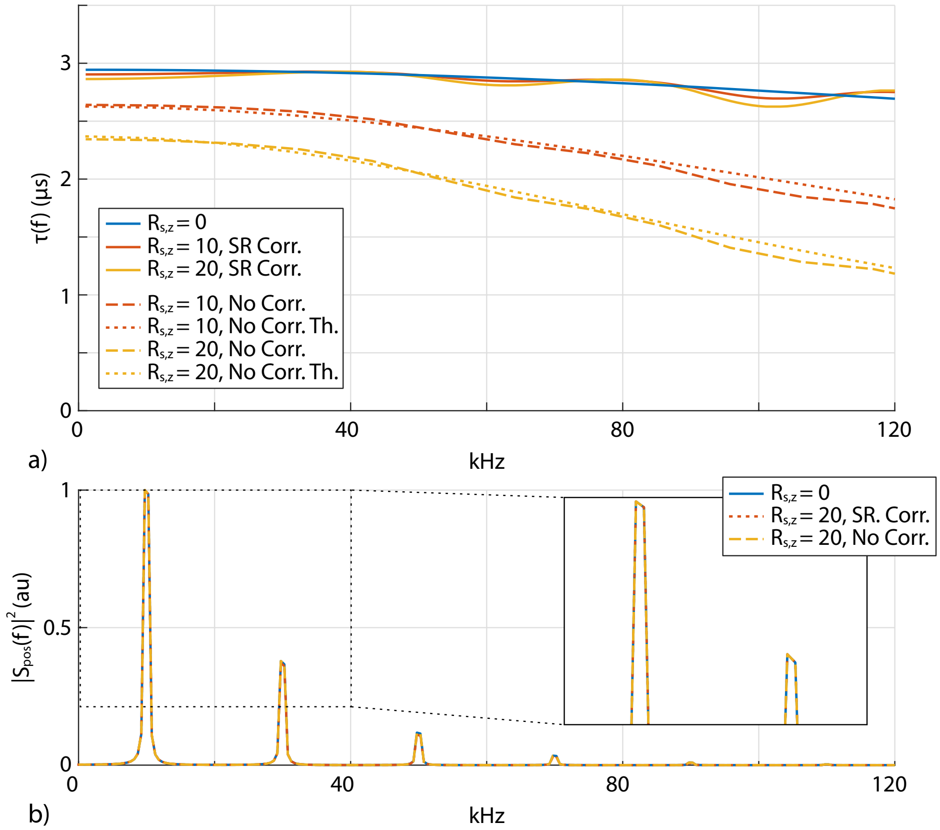

Figure 3.3: (a) $\tau(f)$ for $R_{s,z} = 10$ and 20 T/s and (b) normalized power spectrum of the positive half-cycle before and after SR correction for $R_{s,z} = 20$ T/s. The SR-corrected $\tau(f)$ (solid lines) closely follows the reference case of $R_{s,z} = 0$, while the non-corrected $\tau(f)$ (dashed lines) shows increasing levels of underestimation at higher frequencies and closely follows the theoretical (Th.) $\tau_d(f)$ from Eq. 17 (dotted lines). The power spectra match closely. Simulations utilized a point source MNP with $\tau = 3\,\mu$s.

For $s(t)$ in Fig. 3.2.(b), the relaxation effect causes a separation of the positive and mirrored negative signals in the direction opposite to that caused by the

SR. The relaxation effect also broadens the signal along the scanning direction. Directly computing τ using this distorted signal yields $\hat{\tau} = 1.85$ μs, a significant underestimation. After applying SR correction, the amplitudes of the positive and negative signals match and the effective delay between them gets visibly larger. Then, computing τ for the SR-corrected signal gives $\hat{\tau} = 2.89$ μs, a close match to the actual value of $\tau = 3$ μs. Finally, applying deconvolution using this $\hat{\tau}$ recovers the underlying mirror symmetry of the MPI signal.

In Fig. 3.3, $\tau(f)$ and power spectrum are shown before and after SR correction for $R_{s,z} = 10$ and 20 T/s. Here, the results for $R_{s,z} = 0$ are provided as the references without any FF-induced distortions. As seen in Fig. 3.3.(a), the SR-corrected $\tau(f)$ closely follows the reference, whereas the non-corrected $\tau(f)$ shows increasing levels of underestimation at higher frequencies and closely follows the theoretical $\tau_d(f)$ from Eq. (3.15). Here, the ripple effect on SR-corrected $\tau(f)$ at $R_{s,z} = 10$ and 20 T/s is caused by the digital manipulations and temporal windowing of the signal. When the FFP speed is more strongly dominated by the DF (i.e., for smaller $R_{s,z}$), these ripples flatten and SR-corrected $\tau(f)$ converges to the reference. Nevertheless, since TAURUS applies an averaging of $\tau(f)$ weighted by the magnitude spectrum, the ripples in $\tau(f)$ at high frequencies have a relatively minor effect on the final estimated τ. In Fig. 3.3.(b), the normalized power spectrum of $s_{\text{pos}}(t)$ is shown, where there is negligible difference between the SR-corrected and non-corrected cases and the reference.

3.2.2 Extensions to Multi-dimensional FFs

The trajectory in Eq. (4.1) covers the FOV as a ”line-by-line trajectory” (LLT), with overlapping pFOVs along the z-direction and discrete steps in the x- and y-directions. Due to the continuously ramping FF, this trajectory is already much faster than PWT. For example, for the FFP scanner used in this work with $G_z = 2.4$ T/m, even a relatively modest SR of $R_{s,z} = 4$ T/s corresponds to 0.83 m/s speed, which can cover a human-length line segment in approximately 2 seconds.

To cover a 2D or 3D FOV continuously, time-varying FFs, $B_{F,i}(t)$, can be utilized in all directions, i.e.,

$$\boldsymbol{x}_s(t) = \begin{bmatrix} {}^{B_{F,x}(t)}/_{G_x} \\ {}^{B_{F,y}(t)}/_{G_y} \\ {}^{B_{F,z}(t)}/_{G_z} \end{bmatrix} + \begin{bmatrix} 0 \\ 0 \\ \frac{B_p}{G_z} cos(2\pi f_d t) \end{bmatrix}. \tag{3.16}$$

Defining $R_{s,i}(t) = \frac{d}{dt} B_{F,i}(t)$ as the SR for the FF along each direction, the assumption in Eq. (3.2) can be generalized as:

$$B_p 2\pi f_d \gg \max_t \{ |R_{s,z}(t)| \}, \ \forall t \in [0, T_s]. \tag{3.17}$$

Here, T_s is the total scan time. For example, for $B_p = 15$ mT, $f_d = 10$ kHz, and $R_{s,z} = 20$ T/s, Eq. (3.17) yields a ratio of 47 between the left- and right-hand sides of the inequality. Therefore, adopting the 20 T/s safety limit of MRI gradient fields to FFs [89, 82], it can be concluded that the DF dominates the FFP speed for all practical purposes.

3.2.3 Least Squares Extensions to TAURUS

The frequency domain division in Eq. (3.10) makes TAURUS susceptible to division by a small number or zero under the presence of noise and interference. Therefore, Eq. (3.10) can be casted as a weighted least squares (WLS) problem by first expressing it as a vector relation:

$$\mathbf{a}\tau = \mathbf{b}, \tag{3.18}$$

where $\mathbf{a}, \mathbf{b} \in \mathbb{C}^{K \times 1}$ such that:

$$\mathbf{a} = i2\pi k\Delta f \big(S^*_{\text{pos,c}}(k\Delta f) - S_{\text{neg,c}}(k\Delta f) \big), \tag{3.19a}$$

$$\mathbf{b} = S^*_{\text{pos,c}}(k\Delta f) + S_{\text{neg,c}}(k\Delta f). \tag{3.19b}$$

Here, $k = 0, 1, ..., K-1$ with $K = f_s/\Delta f$, where f_s is the sampling frequency and Δf is the resolution in frequency domain. WLS-TAURUS can then be written as:

$$\tau = (\mathbf{a}^{\mathrm{H}}\mathbf{W}\mathbf{a})^{-1}\mathbf{a}^{\mathrm{H}}\mathbf{W}\mathbf{b}, \tag{3.20}$$

where $\mathbf{W} \in \mathbb{R}^{K\times K}$ is a diagonal weighting matrix with $W_{k,k} = |S_{\mathrm{pos,c}}(k\Delta f)|^2$, and the superscript H denotes Hermitian transpose. As seen in Fig. 3.3.(b), this weighting is similar to harmonic selection, but provides better generalization when the signal energy shows variations across harmonics depending on the MNP distribution, or when the signal energy spreads around the harmonics at high SRs. WLS-TAURUS avoids the problem of division by a small number or zero, and is expected to provide robustness against noise.

3.2.4 Signal Replication for Increased TAURUS Performance for Time-varying FFs

In Eq. (3.10), directly using the SR-corrected positive and negative signals, $s_{\mathrm{pos,c}}(t)$ and $s_{\mathrm{neg,c}}(t)$, results in a poor frequency resolution of $\Delta f = 2f_d$ (i.e., the inverse of a half DF period). To improve the frequency resolution, each period of the SR-corrected signal was first replicated N_{rep} times, then concatenated with the positive signal on the right side for $s_{\mathrm{pos,c}}(t)$ and with the negative signal on the left side for $s_{\mathrm{neg,c}}(t)$ to yield the extended versions. This procedure improves the frequency resolution to $\Delta f = 2f_d/(2N_{\mathrm{rep}} + 1)$.

Example extended signals and the corresponding $\tau(f)$ for N_{rep} values of 0 and 4 at $R_{s,z} = 20$ T/s are given Fig. 3.4.(a). Note that the underlying mirror symmetry feature still applies for these extended signals. Next, the effect of N_{rep} on the $\tau(f)$ and the power spectra is shown in Fig. 3.4.(b). As clearly seen in the power spectra, the frequency resolution increases as N_{rep} increases. In Fig. 3.4.(c), the performances of SR-corrected TAURUS and WLS-TAURUS are evaluated as a function of $N_{\mathrm{rep}} \in [0,\ 10]$ for the noise-free case and for relatively low signal-to-noise ratios (SNRs) of 2 and 10. The estimation error as a function of N_{rep} indicates that $N_{\mathrm{rep}} < 3$ results in poor performance especially at SNR = 2. The performances of TAURUS and WLS-TAURUS both converge to a constant level for $N_{\mathrm{rep}} > 5$, independent of the noise level. Therefore, for the rest of this work, $N_{\mathrm{rep}} = 6$ was utilized.

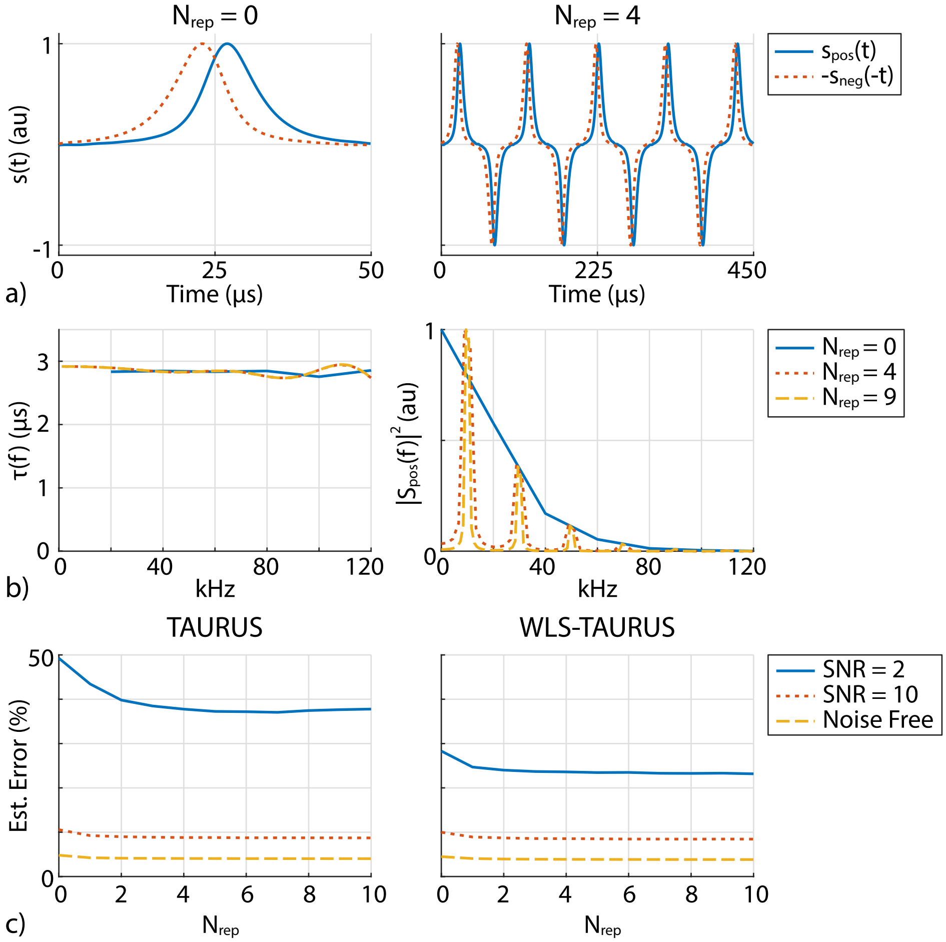

Figure 3.4: Effects of signal replication on estimation error. (a) The positive and mirrored negative signals for $N_{\text{rep}} = 0$ (i.e., no replication) and $N_{\text{rep}} = 4$. (b) $\tau(f)$ and power spectra for different N_{rep} values. (c) Estimation error as a function of N_{rep} at different SNR levels for SR-corrected TAURUS and WLS-TAURUS.

3.3 Methods

3.3.1 1D and 2D Simulations

The MPI simulations were carried out using a custom toolbox in MATLAB (Mathworks, Natick, MA). The parameters were chosen to mimic the experiments performed on an in-house MPI system: $(-4.8,\ 2.4,\ 2.4)$ T/m SF gradients in x-, y- and z-directions, 1D DF along the z-direction with $f_d = 10$ kHz and $B_p = 15$ mT, creating a pFOV of $W_p = 12.5$ mm. A homogeneous receive coil along the z-direction was utilized. The core MNP diameter, d, was assumed to be 25 nm, a realistic value based on the literature [130, 131]. To simulate the continuous-time nature of the physical world, the MNP responses were first generated at 100 MS/s, and then downsampled to 2 MS/s to generate the MPI signals. To emulate the direct feedthrough filtering utilized in the experiments, a zero-phase finite impulse response (FIR) high-pass filter (HPF) with a cut-off frequency of $1.5f_d$ was utilized. Finally, before applying TAURUS, the resulting signals were upsampled at 10 MHz to increase computational accuracy [114]. The details of each simulation are explained in detail below.

3.3.1.1 Slew Rate Robustness

The SR robustness of the proposed method was evaluated for $R_{s,z} \in [0,\ 20]$ T/s and $R_{s,x} \in [0,\ 20]$ T/s, where the estimation performances of the no correction and SR correction cases were compared, using WLS-TAURUS. The proposed SR correction in Eq. (3.9) incorporates a time-shift correction and an amplitude correction. Therefore, the performances of the no correction, only amplitude correction, only time-shift correction, and full SR correction cases were also evaluated for $R_{s,z} \in [0,\ 20]$ T/s, using WLS-TAURUS. For these simulations, a point source MNP distribution with $\tau = 3$ μs positioned at the origin with the core diameter of 25 nm was utilized.

3.3.1.2 Robustness against MNP Characteristics

Robustness of the proposed method against d and τ was evaluated for $d \in [15,\ 35]$ nm and $\tau \in [2, 4]$ μs, and SR-corrected TAURUS and WLS-TAURUS were compared. The range for d was chosen based on the literature [130], and the range for τ was based on earlier TAURUS results using similar DFs [114]. These simulations utilized a point source MNP distribution positioned at the origin, with $R_{s,z} = 20$ T/s and $R_{s,x} = 0$ T/s.

3.3.1.3 Noise Robustness

Monte Carlo simulations were performed to compare the noise robustness of TAURUS and WLS-TAURUS, for $SNR \in [2,\ 20]$ and $R_{s,z} \ \in \ [0,\ 20]$ T/s. Accordingly, at a given SNR and $R_{s,z}$, simulations were repeated numerous times and the estimation errors for SR-corrected TAURUS and WLS-TAURUS were averaged across the repetitions. In each repetition, a different instance of white Gaussian noise with zero mean and a given standard deviation (STD) was added to the MPI signal as

$$s_k(t) = s(t) + n(t), \quad n(t) \sim \mathcal{N}(0, \sigma^2), \tag{3.21}$$

where k is the repetition index, $s(t)$ is the noise-free MPI signal before direct feedthrough filtering, and $n(t)$ is the noise process. The noise STD was set as the maximum signal intensity of $s(t)$ divided by the targeted SNR level, i.e., peak SNR:

$$\sigma = \frac{max\{|s(t)|\}}{SNR}. \tag{3.22}$$

Here, SNR is a numeric value that determines the standard deviation of the white Gaussian noise. The number of repetitions was set to 10^4 for $SNR \leq 5$, and 10^3 for $SNR > 5$ to ensure accurate estimation of performances. A point source MNP distribution with $\tau = 3$ μs positioned at the origin was utilized.

3.3.1.4 Color MPI Simulations

Finally, color MPI simulations were performed to evalute the performance of the proposed method. A phantom containing 6 MNP distributions with τ =[2, 2.4, 2.8, 3.2, 3.6 4] μs was created. Each MNP distribution had a size of 2 mm×2 mm. A 5 cm×6 cm FOV in the x-z plane was scanned using 3 different trajectories:

Piecewise Trajectory (PWT): The FFs along the x- and z-directions were stepped to cover the FOV at 100×100 points in the x-z plane, providing 95.2% overlap between the consecutive pFOVs along the z-direction. An MPI signal of 10 ms duration was simulated at each point, resulting in an active scan time of 100 s for the entire trajectory.

Line-by-line Trajectory (LLT): A linearly ramping FF in the z-direction was utilized with $R_{s,z} = 4$ T/s to cover each line in 36 ms, with 98.7% overlap between the consecutive pFOVs along the z-direction. The FF along the x-direction was stepped to cover the x-direction at 100 equally spaced lines, resulting in an active scan time of 3.6 s.

2D Triangle Trajectory (2DTT): To cover the 2D FOV continuously, a linearly ramping FF in the z-direction was utilized. A triangle wave FF was applied along the x-direction, formulated as follows:

$$x(t) = \frac{\text{FOV}_x}{\pi} sin^{-1}\big(sin(2\pi f_{\mathsf{T}} t)\big), \;\; t \in [0, T_s). \tag{3.23}$$

Here, $f_{\mathsf{T}} = R_{s,x}/(2\text{FOV}_x G_x)$ is the frequency of the triangle wave and scan time $T_s = \text{FOV}_z/(R_{s,z}/G_z)$. $R_{s,z} = 0.5$ T/s and $R_{s,x} = 20$ T/s were chosen to densely cover the whole FOV. There was no explicit overlap among the neighboring pFOVs due to the continuous movement along the x-direction. The resulting active scan time was 0.288 s.

Note that the active scan times listed above do not include the idle times of PWT and LLT during which the FFP position is stepped. For example, traversing each line back at the same SR of $R_{s,z} = 4$ T/s would automatically double the total scan time of LLT to 7.2 s. In contrast, 0.288 s active scan time for 2DTT is directly equal to the total scan time, as the whole FOV is scanned continuously in a single shot.

3.3.2 Imaging Experiments

Color MPI imaging experiments were performed on the in-house FFP MPI scanner shown in Fig. 3.5.(a), using 3 different trajectories. This scanner had $(-4.8,\ 2.4,\ 2.4)$ T/m SF gradients in the x-, y- and z-directions, and featured a free bore size of 1.9 cm and air cooling to prevent system heating. Both the drive and receive coils were oriented along the z-direction. To minimize the direct feedthrough, the receive coil was designed as a tunable 3-section gradiometric coil. Instead of utilizing FF coils to globally move the FFP, this scanner used a three-axis linear actuator (Velmex BiSlide), with a maximum speed of 38.1 mm/s in all axes, corresponding to $R_{s,z} = 0.091$ T/s. The other details of the scanner can be found in [114, 104].

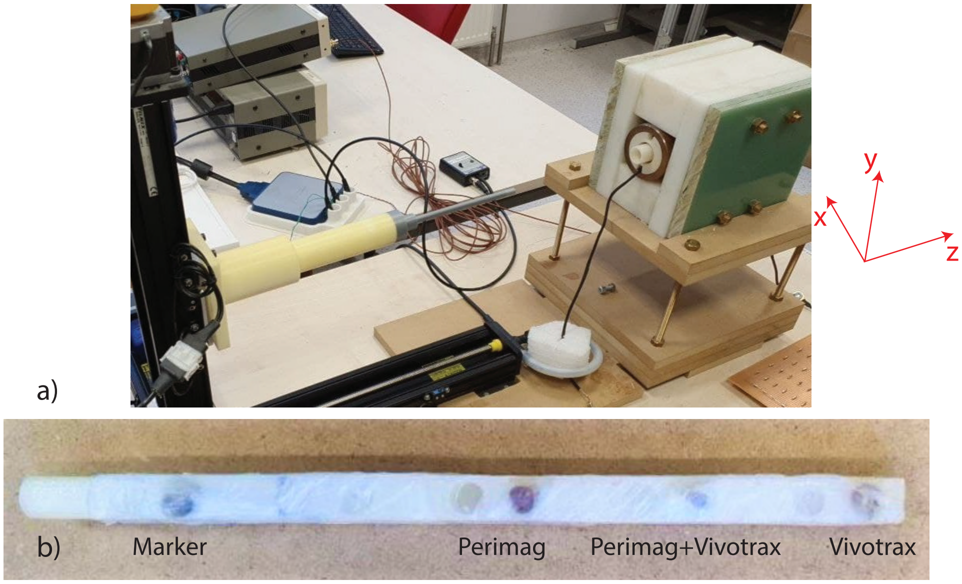

Figure 3.5: (a) In-house FFP MPI scanner with $(-4.8,\ 2.4,\ 2.4)$ T/m SF gradients and 1D DF along the z-direction at 10 kHz with a three-axis linear actuator was utilized to move the FFP globally, instead of using FFs. (b) The imaging phantom contained Perimag, Vivotrax, their mixture, and a marker.

The flow diagram of the experimental process is presented in Fig. 3.8.(a). For precise synchronization of the signal transmission/reception and the linear actuator movement, a digital trigger was sent from the VXM-2 motor controller of the actuator to a data acquisition card (DAQ) (NI PCIe-6374). The DAQ card sent the DF signal to the power amplifier (AE Techron 7224), which then sent it to the drive coil via an impedance matching circuitry tuned to $f_d =$ 10 kHz. A current probe (PEM LFR 06/6/300) was used for calibrating B_p. The received signal was pre-amplified using a low-noise amplifier (SRS SR560) and then sampled at 2 MS/s using the DAQ.

3.3.2.1 Trajectory Specifications

A 2D FOV of 0.7 cm×12.7 cm in the x-z plane was scanned using 3 different trajectories, shown in Fig. 3.6 and 3.7. The experiments utilized $f_d = 10$ kHz and $B_p = 15$ mT, resulting in a pFOV size of W_p =12.5 mm. For direct feedthrough compensation, baseline measurements were acquired before and after each line for PWT and LLT, and before and after the entire trajectory for 2DTT.

PWT: The FOV was divided into 11×100 points in the x-z plane, providing 89.84% overlap between the consecutive pFOVs. A 150 ms signal was acquired for each pFOV, resulting in an active scan time of 165 s. Due to the idle times needed for actuator motion, the total scan time was approximately 46 min.

LLT: The x-direction was divided into 11 equally spaced lines. For the z-direction, the actuator was moved continuously at its maximum speed of 38.1 mm/s, corresponding to $R_{s,z} = 0.091$ T/s for $G_z = 2.4$ T/m. This relatively low $R_{s,z}$ resulted in 99.97% overlap between the consecutive pFOVs. Each line was covered in 3.46 s, resulting in an active scan time of 38 s. The total scan time was 76 s due to the idle times needed for the backward actuator movement along each line.

2DTT: A continuous triangle wave movement with $R_{s,x} = 0.061$ T/s and $R_{s,z} = 0.03$ T/s was applied using Eq. (3.23). The active scan time was 19.8 s, with no idle time.

3.3.2.2 Phantom Preparation

As shown in Fig. 3.5.(b), an imaging phantom was prepared with 3 different samples, containing Perimag (Micromod GmbH), Vivotrax (Magnetic Insight Inc.) and their equal volume mixture. The samples were placed with 2.3 cm center-to-center separations. Each sample had 3 mm diameter in the x-z plane and contained a total volume of 20 μL. Perimag (17 mg Fe/mL undiluted concentration) was diluted 10.5 times to approximately equalize its signal level to that

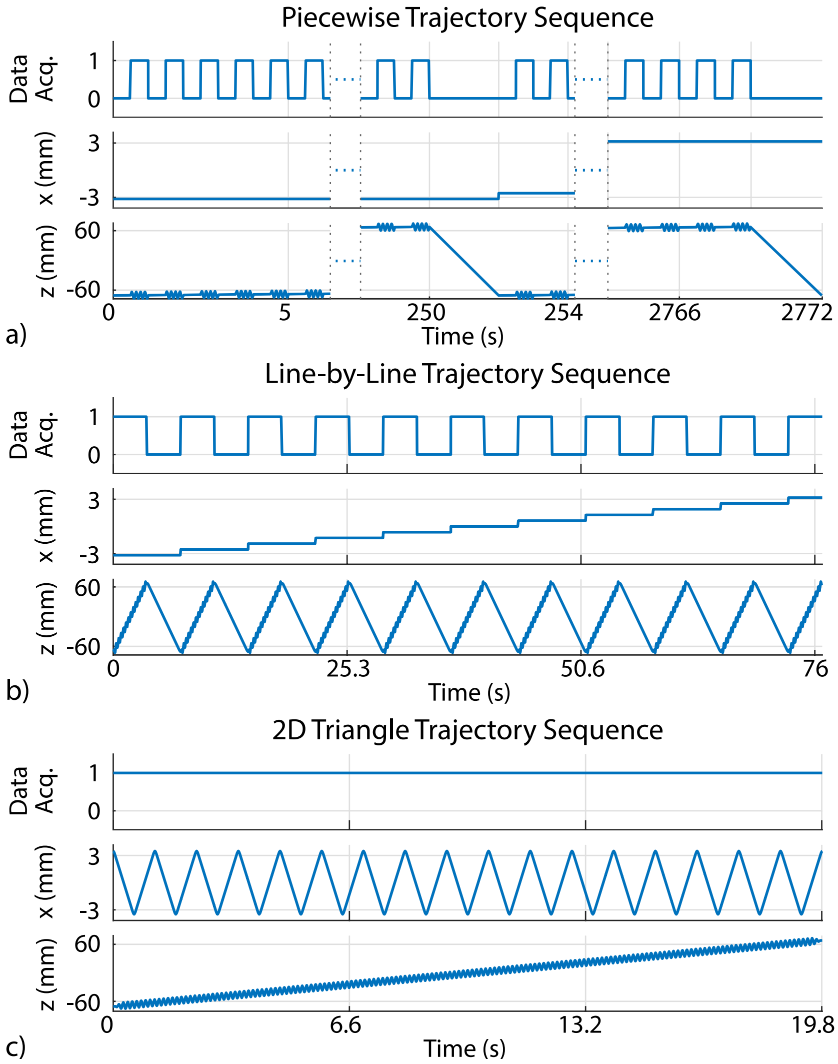

Figure 3.6: Trajectories with the superimposed 1D DF along the z-direction. (a) PWT, with stepped x- and z- directions. (b) LLT, with stepped x-direction and a linear z-direction. (c) 2DTT with a triangle-wave x-direction and a linear z-direction.

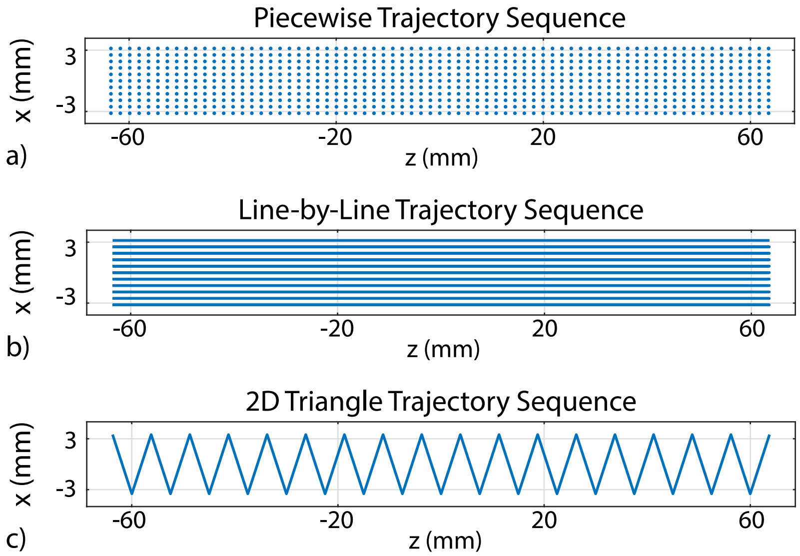

Figure 3.7: Focus field movements of the trajectories on x-z plane for, (a) PWT, (b) LLT, and (c) 2DTT. The trajectories do not reflect the DF.

of Vivotrax (5.5 mg Fe/mL undiluted concentration). For computing signal timing (see Sec. 3.3.2.4), an additional marker sample containing 10 μL undiluted Perimag was placed at a 4.6 cm separation from the leftmost sample.

3.3.2.3 Signal Preprocessing

As outlined in Fig. 3.8.(b), the received and baseline signals were individually low pass filtered using a zero-phase FIR filter with a cut-off frequency at 120 kHz to denoise the signal and remove the self-resonance of the receive coil at 280 kHz. Potential system drifts (e.g., due to heating or vibration) can cause slight delays between these two signals. This delay was negligibly small for PWT due to the short DF signals separated by extensive idle times that allowed system cooling. For LLT and 2DTT, the delay was more prominent due to the longer DF signals. The relative delay was computed by first upsampling the received and baseline signals at 100 MHz sampling rate, followed by a cross-correlation operation. The baseline signal was then time-shifted and subtracted from the received signal. Finally, the direct feedthrough at the fundamental harmonic was filtered out using a zero-phase FIR HPF with a cut-off frequency of $1.5f_d$.

3.3.2.4 Digital Fine-Tuning of Signal Timing

TAURUS requires a precise (sub-sample level) adjustment of signal timing, as unaccounted delays can cause a bias in $\hat{\tau}$. The signal timing, t_i, of the preprocessed signal was fine tuned using the marker signal. To achieve sub-sample precision, first the signal was upsampled at 100 MHz sampling rate. The tuning process took advantage of the underlying mirror symmetry: when $r_\tau(t)$ computed at the correct t_i is used to deconvolve the signal, the mirror symmetry should be achieved [114], i.e.,

$$\hat{t}_i = \underset{t_\mathrm{i}}{\operatorname{argmin}}\ \mathrm{MSE}(s_{\mathrm{pos,d}}(t), -s_{\mathrm{neg,d}}(-t)). \tag{3.24}$$

Here, $\hat{t}_i$ is the estimated signal timing that minimizes the mean square error (MSE) in mirror symmetry. In addition, $s_{\mathrm{pos,d}}(t)$ and $s_{\mathrm{neg,d}}(t)$ denote the positive and negative signals after deconvolution with $r_\tau(t)$ computed at t_i, respectively. Finally, the estimated $\hat{t}_i$ was applied to the entire signal. As outlined in Fig. 3.8.(b), the resulting signal is then fed to the image reconstruction step.

3.3.3 Color MPI Image Reconstruction

Color MPI image reconstruction was composed of three steps: MPI image reconstruction, $\hat{\tau}$ map reconstruction, and color overlay formation.

MPI Image Reconstruction: The MPI images for PWT and LLT were reconstructed using Partial FOV Center Imaging (PCI) reconstruction [127]. PCI requires the pFOV centers to be aligned on a line and to have a high overlap percentage, and hence is suitable for PWT and LLT. Since 2DTT does not have any explicit overlap between pFOVs, PCI is not directly applicable. Taking advantage of the continuous signal acquisition of this trajectory, Harmonic Dispersion X-space (HD-X) reconstruction was utilized [132]. Since the data points in 2DTT were on a non-Cartesian grid, an automated gridding algorithm for non-Cartesian MPI reconstruction was utilized on the HD-X data [126]. This gridding algorithm automatically tuned all reconstruction parameters, including the grid size.

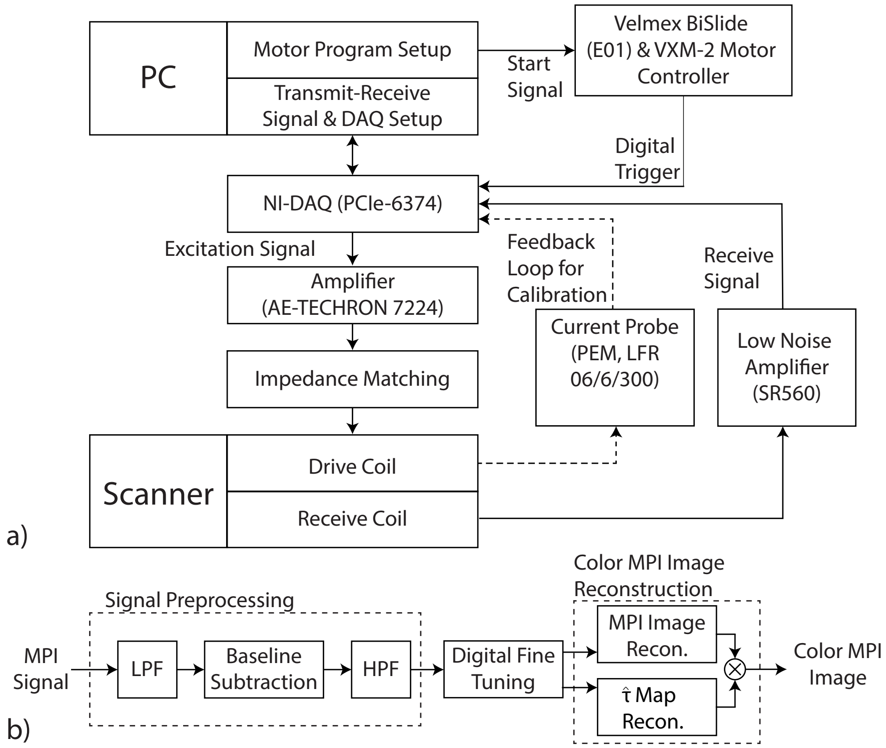

Figure 3.8: (a) The flow diagram of the experimental process. A digital trigger from the VXM-2 motor controller was sent to the DAQ for synchronization. (b) The digital signal processing and image reconstruction stages for color MPI.

To reduce the blurring introduced by the gridding operation, the Cartesian output image was deconvolved with the gridding kernel using the Lucy-Richardson deconvolution[133]. The final reconstructed images had 500×600 pixels for the simulations and 200×2133 pixels for the imaging experiments.

$\hat{\tau}$ **Map Reconstruction**: After SR correction of each DF period, $\hat{\tau}$ was estimated using WLS-TAURUS with $N_{\text{rep}} = 6$. The estimated $\hat{\tau}$ values were placed on the corresponding pFOV center locations to form a $\hat{\tau}$ map. For 2DTT, the above-mentioned gridding algorithm was utilized to grid the $\hat{\tau}$ values to a Cartesian grid [126]. In the background regions, $\hat{\tau}$ can have unexpectedly high or low values due to low SNR. To ensure that these outlier $\hat{\tau}$ values do not contaminate the $\hat{\tau}$ map, the gridding kernel was reduced to one-fourth of that used during image reconstruction. Finally, the $\hat{\tau}$ map was interpolated to match the size of the MPI image. To suppress the noise-like $\hat{\tau}$ values in the background regions, the $\hat{\tau}$ map was multiplied with a binary mask of the MPI image, with a threshold of 10% of the maximum pixel intensity.

Color Overlay Formation: The $\hat{\tau}$ maps were overlayed with the reconstructed MPI images by multiplying the RGB pixel intensities of the two images, channel by channel.

3.4 Simulation Results

3.4.1 SR Robustness Results

The slew rate robustness of the proposed method is presented in Fig. 3.9.(a) as a function of $R_{s,z}$ and $R_{s,x}$, ranging between 0-20 T/s. Here, both the no correction and SR correction results utilized WLS-TAURUS. These results indicate that the estimation error does not depend on $R_{s,x}$, but is rather dominated by $R_{s,z}$ for the no correction case, reaching 37% error at $R_{s,z} = 20$ T/s. SR correction successfully reduces the estimation error to below 3.6% at all $R_{s,z}$ and $R_{s,x}$ values tested.

Figure 3.9.(b) shows the estimation error at $R_{s,x} = 20$ T/s as a function of $R_{s,z}$. Even at this large $R_{s,x}$, SR correction maintains a low estimation error at all $R_{s,z}$ values tested. Next, Fig. 3.9.(c) shows the estimation error at $R_{s,z} = 20$ T/s, displaying a less than 0.05% increase as a function of $R_{s,x}$ for both the no correction and SR correction cases.

The component-wise performances of the proposed SR correction method were also evaluated for $R_{s,z}$ ranging between 0-20 T/s (results not shown). Amplitude correction alone had minimal effect (less than 0.01%) on the estimation performance with respect to the no correction case. In contrast, time-shift correction alone provided a performance improvement that is only slightly (less than 0.06%) lower than the full SR correction case.

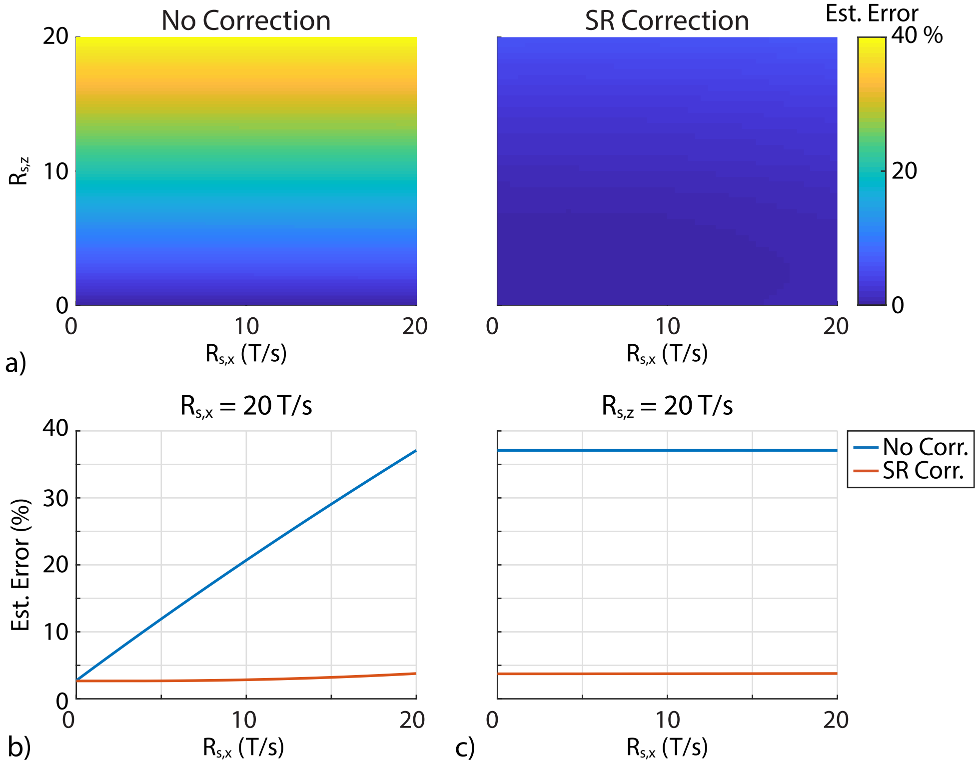

Figure 3.9: SR robustness results. The estimation error (a) as a function of $R_{s,x}$ and $R_{s,z}$ for no correction and SR correction, (b) as a function of $R_{s,z}$ for $R_{s,x} = 20$ T/s, and (c) as a function of $R_{s,x}$ for $R_{s,z} = 20$ T/s. SR correction reduces the estimation error to below 3.6% at all $R_{s,z}$ and $R_{s,x}$ values.

3.4.2 MNP Characteristics Robustness Results

The robustness against MNP characteristics for SR-corrected TAURUS and WLS-TAURUS are given in Fig. 8 for d ranging between 15-35 nm and τ ranging between 2-4 μs. Figure 8 shows comparable performances for both methods, with estimation errors below 3.7% for $d > 19$ nm, nearly independent of τ. The estimation error is approximately 8.6% at $d = 15$ nm and $\tau = 2$ μs, whereas it decreases down to 3.1% for TAURUS and 2.9% for WLS-TAURUS at $d = 35$ nm and $\tau = 4$ μs.

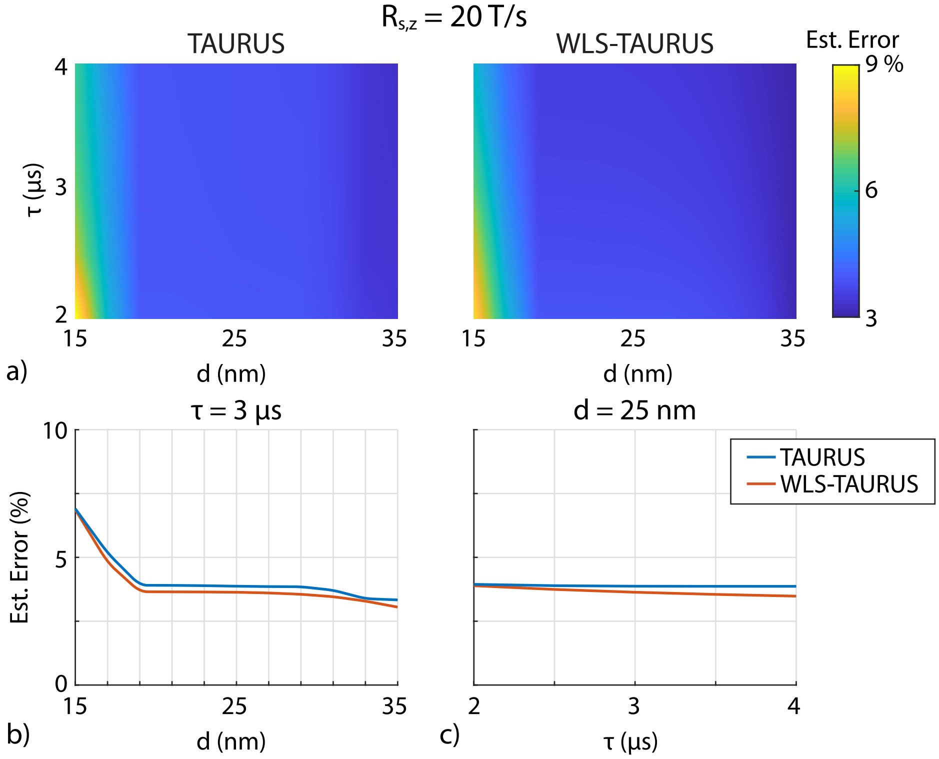

Figure 3.10: Results for robustness against MNP characteristics. The estimation error for SR-corrected TAURUS and WLS-TAURUS (a) as a function of d and τ, (b) as a function of d for $\tau = 3\mu$s, and (c) as a function of τ for $d = 25$ nm. Both TAURUS and WLS-TAURUS show low estimation error for $d > 19$ nm.

3.4.3 Noise Robustness Results

Noise robustness results for SR-corrected TAURUS and WLS-TAURUS are given in Fig. 3.11 for SNR ranging between 2-20 and $R_{s,z}$ ranging between 0-20 T/s. This analysis did not include $R_{s,x}$, as Fig. 3.9 indicated that $R_{s,x}$ does not have an impact on the estimation error. As seen in Fig. 3.11.(a), the estimation error after SR correction is almost independent of $R_{s,z}$, but depends largely on the noise level. At high SNR levels, WLS-TAURUS provides a relatively small improvement over TAURUS. At low SNR levels, TAURUS shows high estimation errors, particularly for SNR < 5. In contrast, WLS-TAURUS maintains robustness against noise even at SNR $= 2$.

In Fig. 3.11.(b), SR-corrected $\tau(f)$ in Eq. (3.10) is plotted at 4 different SNR

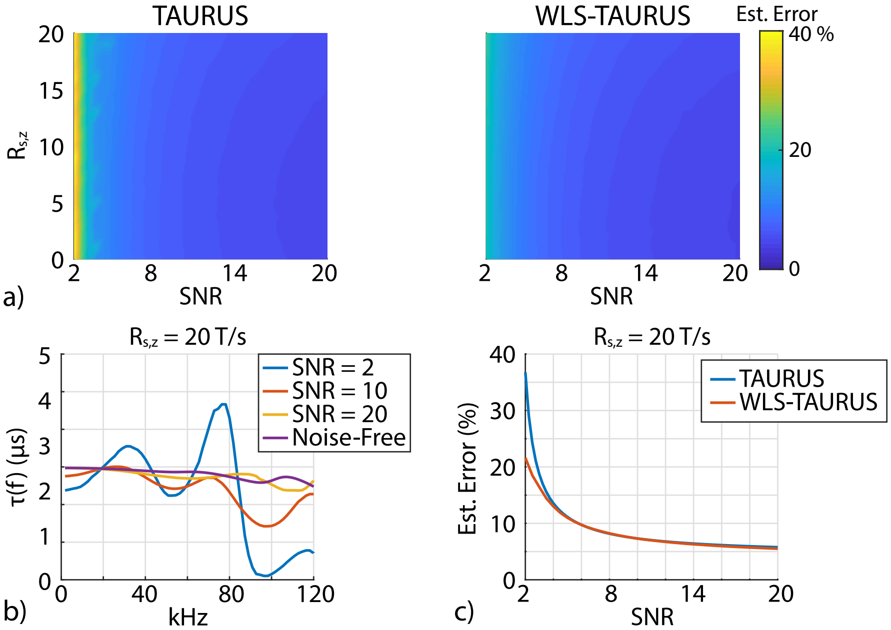

Figure 3.11: Noise robustness results. (a) The estimation error for SR-corrected TAURUS and WLS-TAURUS with respect to SNR and $R_{s,z}$. (b) $\tau(f)$ for 4 different SNR levels at $R_{s,z} = 20$ T/s. (c) TAURUS vs. WLS-TAURUS with respect to SNR at $R_{s,z} = 20$ T/s. WLS-TAURUS shows improved robustness, especially for SNR < 5.

levels at $R_{s,z} = 20$ T/s. At SNR $= 2$, $\tau(f)$ shows large ripple-like deviations from the ideal value of $\tau = 3$ μs. These deviations increase at high frequencies, as the signal energy gets smaller and the computation of $\tau(f)$ gets dominated by noise. In addition, these ripples decrease at high SNR and converge to the noise-free case. As previously shown in Fig. 3.3, the ripples also increase with $R_{s,z}$. Hence, $\tau(f)$ shown for SNR $= 2$ and $R_{s,z} = 20$ T/s corresponds to the most challenging scenario.

Next, Fig. 3.11.(c) shows a direct comparison of TAURUS and WLS-TAURUS at $R_{s,z} = 20$ T/s as a function of SNR, where the improved noise robustness of WLS-TAURUS is clearly visible for SNR < 5. At SNR $= 2$, the estimation errors for TAURUS and WLS-TAURUS are 37% and 21%, respectively. At SNR $=$ 20, the estimation errors fall down to 5.5% and 5.0% for TAURUS and WLS-TAURUS, respectively. In comparison, the estimation errors are 3.8% and 3.6% in the noise-free case for TAURUS and WLS-TAURUS, respectively.

3.4.4 Color MPI Simulation Results

Figure 3.12 shows the color MPI simulation results for 3 different trajectories. The digital phantom used in these simulations is displayed in Fig. 3.12.(a), with τ values between 2-4 μs. Fig. 3.12.(b), where the error bars denote the mean and STD of the estimation errors in $\hat{\tau}$ within the 2 mm×2 mm region for each MNP distribution. In Fig. 3.12.(c)-(e), the color overlays show comparable performance for PWT, LLT, and 2DTT, despite their vastly different speeds. The estimation performances are compared quantitatively in

As seen in these results, 2DTT has the best performance, whereas LLT shows slightly improved performance over PWT. The mean estimation errors across all MNPs were 1.5±0.2%, 0.6±0.2% and 0.4±0.4% for PWT, LLT, and 2DTT, respectively. Figure 3.12.(b) also demonstrates the importance of SR correction: the estimations errors were 9.0±1.2% and 2.2±1.8% for the non-corrected cases of LLT and 2DTT, respectively. Here, consistent with the results in Fig. 3.9, the non-corrected case of LLT displayed a larger error due to utilizing higher $R_{s,z}$.

Additionally, the results directly reflect the effect of trajectory density and $\hat{\tau}$ map fidelity for the SR-corrected cases. While LLT is denser than PWT along the z-direction, both LLT and PWT are relatively sparse along the x-direction. In contrast, 2DTT provides a dense coverage along both the x- and z-directions, resulting in improved estimation performance.

3.5 Experiment Results

Figure 3.13.(a)-(c) displays the imaging experiment results, showing the reconstructed MPI images, $\hat{\tau}$ maps, and color overlay images for 3 different trajectories. For PWT and LLT, $\hat{\tau}$ shows a large variation along the x-direction due to the low trajectory density in that direction. For 2DTT, $\hat{\tau}$ map is visibly smoother with reduced variations along both x- and z-directions, as this trajectory is considerably denser than the other two trajectories. Since Vivotrax has worse full-width

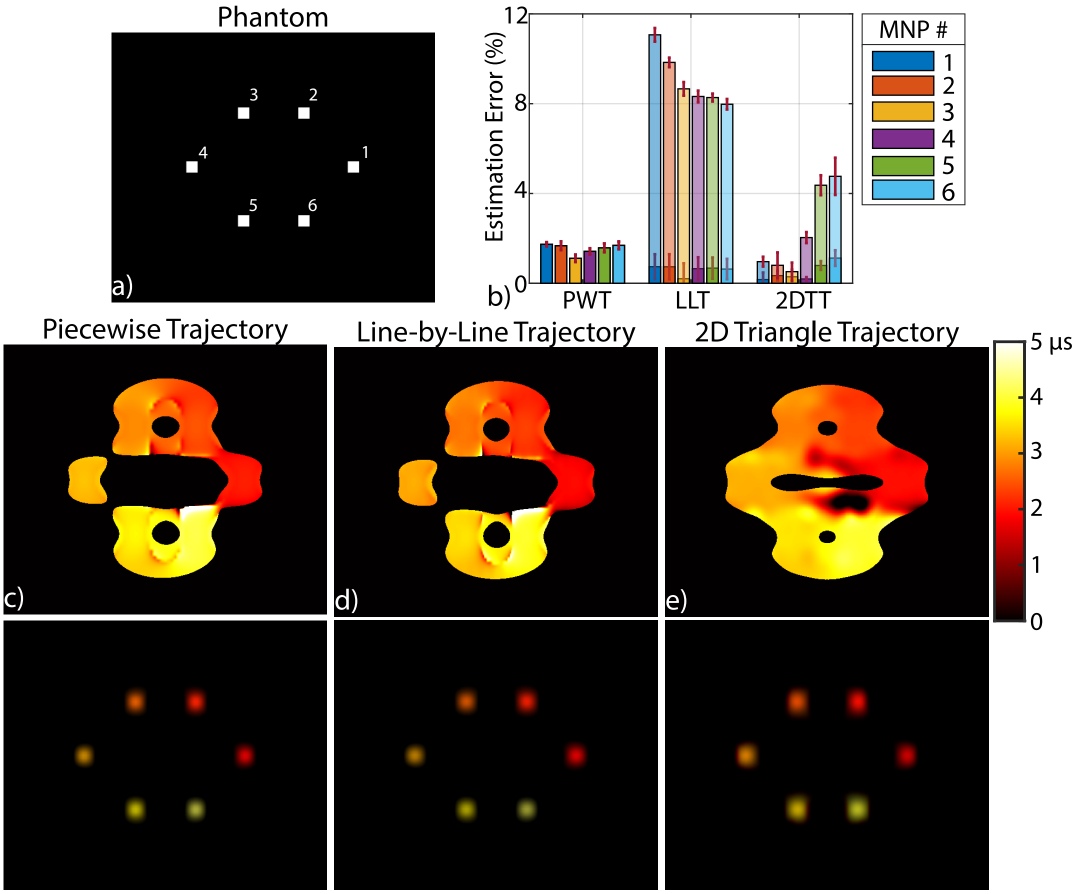

Figure 3.12: Color MPI simulation results for 3 different trajectories. (a) The digital phantom with τ between 2-4 μs. (b) The estimation performances, where the error bars denote the mean and STD of the estimation error in $\hat{\tau}$ for the non-corrected (semi-transparent bars) and SR-corrected (solid bars) cases. SR correction does not apply to PWT. The $\hat{\tau}$ maps (top row) and the corresponding color overlays (bottom row) for (c) PWT, (d) LLT, and (e) 2DTT, showing comparable performance despite their vastly different trajectory speeds. SR correction provides a significant improvement in accuracy. 2DTT shows high accuracy estimation with fast scanning and dense coverage.

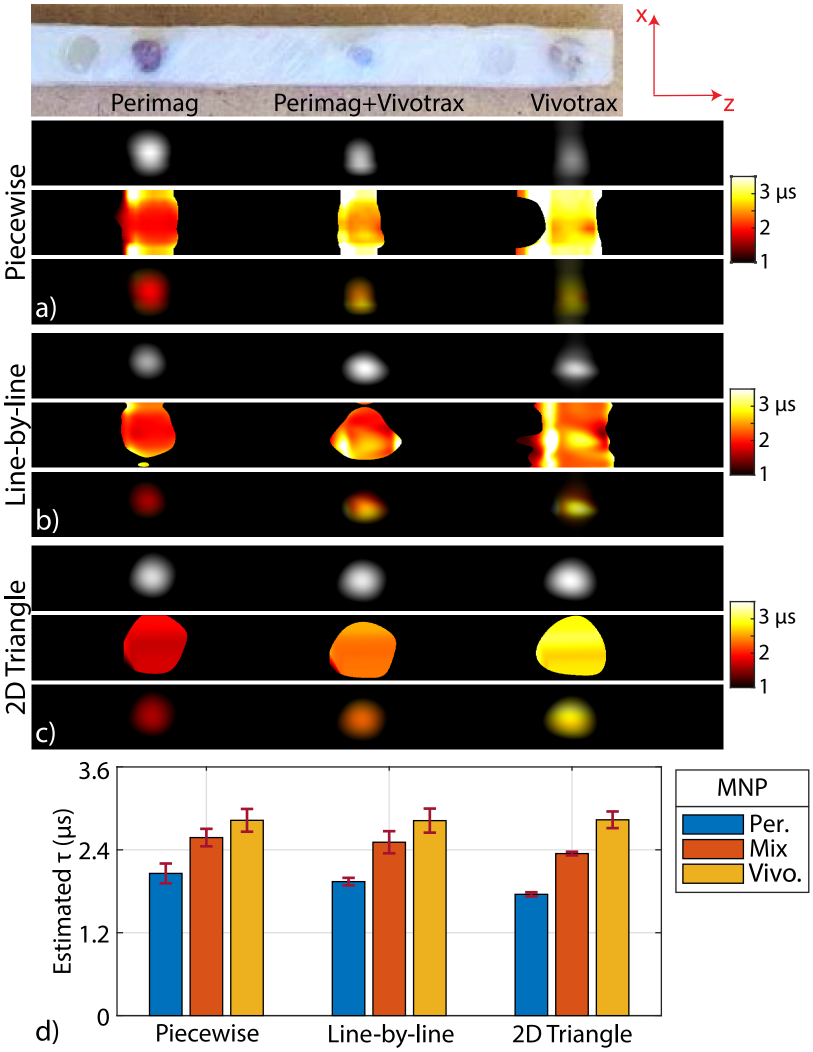

Figure 3.13: Imaging experiment results. The reconstructed MPI images, $\hat{\tau}$ maps, and color overlays for (a) PWT, (b) LLT, and (c) 2DTT. $\hat{\tau}$ map for 2DTT is visibly smoother. (d) The estimated $\hat{\tau}$ for each sample, where the error bars denote the mean and STD within the FWHM region of the respective MPI image for that sample and trajectory. The displayed FOV is 0.7 cm×7.3 cm.

at half-maximum (FWHM) resolution than Perimag, its $\hat{\tau}$ values extend in a wider region along the z-direction [114].

The estimated $\hat{\tau}$ for each sample are given as bar plots in Fig. 3.13.(d). Here, the error bars denote the mean and STD of $\hat{\tau}$ of each sample within the FWHM region of the respective MPI image for that sample and trajectory. For PWT, the $\hat{\tau}$ values were 2.06±0.14 μs, 2.58±0.13 μs, and 2.83±0.16 μs for Perimag, mixture, and Vivotrax, respectively. For LLT, the $\hat{\tau}$ values were 1.94±0.05 μs, 2.51±0.16 μs, and 2.82±0.17 μs for Perimag, mixture, and Vivotrax, respectively. For 2DTT, the $\hat{\tau}$ values were 1.78±0.03 μs, 2.36±0.02 μs, and 2.83±0.12 μs for Perimag, mixture, and Vivotrax, respectively. These results indicate that $\hat{\tau}$ for Vivotrax is consistent, showing less than 1% variation across trajectories. This consistency is potentially due to the worse FWHM resolution of Vivotrax, which provides a paradoxical robustness against the low densities of PWT and LLT along the x-direction. In addition, $\hat{\tau}$ for Perimag is also consistent between PWT and LLT, with only 5.8% difference, as their densities match along the x-direction. In contrast, $\hat{\tau}$ for Perimag for 2DTT is approximately 13.6% and 8.2% lower than for PWT and LLT, respectively. These differences potentially stem from the substantially increased density of 2DTT along the x-direction. For each trajectory, $\hat{\tau}$ for the mixture closely matches the average of $\hat{\tau}$ for Perimag and Vivotrax, as expected [114].

Overall, these results indicate that 2DTT provides reliable $\hat{\tau}$ estimations thanks to its dense coverage, while also providing the shortest scan time among the tested trajectories.

3.6 Discussion

In this work, the techniques that enable relaxation-based color MPI for rapid and multi-dimensional trajectories have been proposed and experimentally demonstrated. The proposed SR correction method provides excellent robustness against FF-induced distortions for a wide range of SR values. Importantly, this method solely depends on the system and trajectory parameters. In addition, using a weighted least squares approach, WLS-TAURUS, successfully improves the noise robustness.

3.6.1 Alternative SR Correction Approaches

The proposed algorithm applies Δt time-shift and α scaling on the negative signal to align it with the positive signal. An alternative approach could be to apply $\Delta t/2$ time-shift and $\sqrt{\alpha}$ scaling on the negative signal and $\Delta t/2$ time-shift and $1/\sqrt{\alpha}$ scaling on the positive signal, so that they meet at the center of the half period. It can be shown that, in theory, this approach yields identical τ as the proposed approach given in Eq. (3.10). In practice also, it provides identical performance to the proposed SR correction, given that FF-induced shifts are within 1% of the DF period even at $R_{s,z} = 20$ T/s.

Another approach could be to fully correct for the time-varying nature of the FF-induced distortions, so that the corrected $s_{\text{adiab}}(t)$ attains perfect mirror symmetry. However, such a correction would essentially stretch or compress one (or both) of the half-cycle signals, perturbing the temporal properties of the relaxation effect in Eq. (2.20). Since frequency-domain relations for TAURUS given in Eqs. (2.21)-(2.22) would no longer apply, this approach is not suitable for relaxation mapping. In contrast, the proposed SR correction preserves the relaxation effects within individual half cycles.

3.6.2 SR Robustness

The simulations presented in this work were based on the in-house MPI scanner, with both the drive and receive coils along the z-direction. As shown in Fig. 3.9, the SR correction is very robust against $R_{s,z}$ and does not depend on $R_{s,x}$. The latter effect stems from two reasons: the collinear PSF is relatively wide along the x-direction [121], and the DF is not along that direction.

For the simulation parameters in this work, the collinear PSF has 1.8 mm and 2.1 mm FWHM along the z- and x-directions, respectively. Even for $R_{s,x} = 20$ T/s, the FFP moves approximately 0.2 mm along the x-direction in half the DF period, which is considerably smaller than the FWHM along that direction. Even in theory, reaching a comparable FWHM would require an effective MNP diameter greater than 55 nm. For the same reasons, $R_{s,y}$ is expected to have a similarly negligible effect.

Visual explanation of robustness against $R_{s,x}$ for the trajectories used in this work is presented in Fig. 3.14. For the simulation parameters in this work, the collinear PSF has 7.5 mm and 7.5 mm FWHM along the z- and x-directions, respectively. The higher FWHM along the x-direction is due to the fact that both the drive and receive coils are oriented along the z-direction. Even for $R_{s,x} = 20$ T/s, the FFP moves approximately 0.2 mm along the x-direction in half the DF period (i.e., between the centers of the positive and the negative half cycles). The fact that this movement is considerably smaller than the FWHM along the x-direction is the fundamental reason behind the robustness against $R_{s,x}$. For the same reasons, $R_{s,y}$ is expected to have a similarly negligible effect.

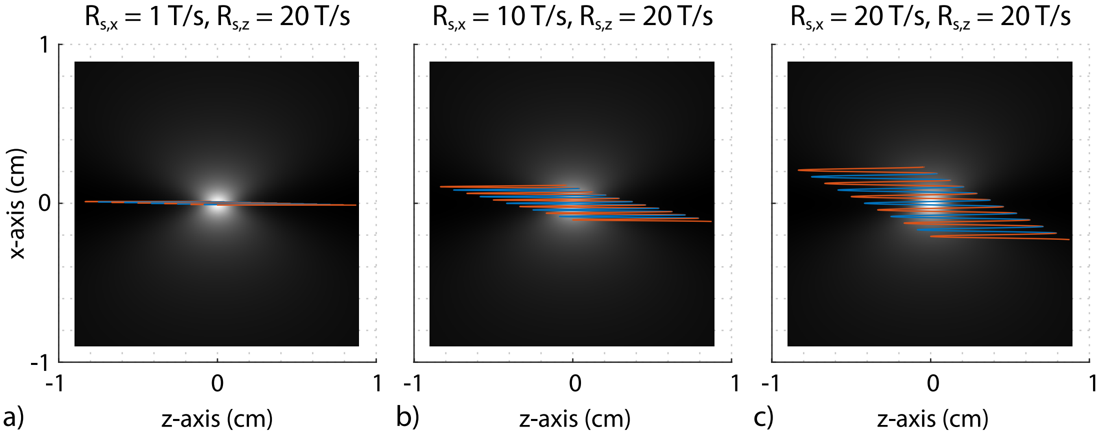

Figure 3.14: The collinear PSF overlayed with a trajectory for $R_{s,z} = 20$ T/s and (a) $R_{s,x} = 1$ T/s, (b) $R_{s,x} = 10$ T/s, and (c) $R_{s,x} = 20$ T/s. The trajectories are displayed for 11 DF periods, with the consecutive periods shown in alternating colors of red and blue. Simulation parameters were $\mathbf{G} = [-4.8, 2.4, 2.4]$ T/m along the x-, y- and z-directions, MNP with 25 nm core diameter, $B_p = 15$ mT, and $f_d = 10$ kHz.

3.6.3 Effects of MNP Diameter

According to the Langevin theory, increasing the MNP diameter or the SF gradients decreases the FWHM of the PSF in all directions [121]. Regardless, the MNP diameter is not expected to have any major effects on the τ estimation performance, as confirmed by the low estimation errors maintained for $d > 19$ nm in Fig. 3.10. First of all, SR correction is independent of the MNP parameters. Secondly, in terms of resolution, increasing the MNP diameter is equivalent to increasing G_z instead. The trajectory can still be kept identical if B_p and $R_{s,z}$ are increased at the same rate as G_z. Because the assumption in Eq. (3.17) remains unchanged, the estimation performance with respect to $R_{s,z}$ should not be affected.

With B_p and G_z fixed, the increase in estimation error for $d < 19$ nm is a result of the excessive widening of the PSF, which causes the MPI image to appear flat within the fixed pFOV size. In general, a flat MNP distribution can be problematic for τ estimation, as it causes the entire signal to fall on the fundamental harmonic. Then, the corresponding pFOV will have low signal after direct feedthrough filtering, despite having a non-zero pixel intensity in the reconstructed MPI image. A potential solution is to fill in the corresponding $\hat{\tau}$ regions using neighboring pFOVs, as proposed in [114]. Another alternative solution is to utilize active cancellation methods to preserve the fundamental harmonic [134, 135].

The effective d for the MNPs in the imaging experiments can be calculated using Fig. 3.13, where the FWHM values along the z-direction are 3.73 mm for Perimag and 4.40 mm for Vivotrax samples. Taking into account the 2.9 mm inner diameter of each sample together with the estimated $\hat{\tau}$ values, the effective MNP diameters are computed as 24.7 nm for Perimag and 21.7 nm for Vivotrax. Note that these diameters are close to the 25 nm diameter used in the simulations, and are well above the 19 nm threshold mentioned above.

3.6.4 Resolution of τ Map

When creating the $\hat{\tau}$ map, a single $\hat{\tau}$ is estimated for each period of the signal and assigned to the center of the corresponding pFOV. Consequently, the resolution of $\hat{\tau}$ map is directly proportional to the trajectory density. For PWT, improving the resolution requires increasing the number of stepped points along both the x- and z-directions, increasing the scan time quadratically for a 2D FOV. For LLT, the resolution along the continuously scanned z-axis is sufficiently high and can be further improved by reducing $R_{s,z}$ (e.g., even at $R_{s,z} = 20$ T/s, the resolution along the z-axis is 0.83 mm for the parameters in this work). However, improving the resolution along the x-direction requires more lines to be scanned, which would increase the scan time linearly for a 2D FOV. In 2DTT, the resolution is considerably improved along the x-direction, but is position dependent. For a fixed scan time and FOV, $R_{s,z}$ and the number of pFOVs are also fixed. Then, a trade-off between the resolutions in the x- and z-directions can be achieved by adjusting $R_{s,x}$. By increasing the scan time and reducing $R_{s,z}$, the overall resolution of $\hat{\tau}$ map can be further improved in both directions.

It should be noted that controlling the trajectory density in a systematic fashion is challenging for 2DTT, as the trajectory parameters are coupled. For example, doubling f_d alone will double the density on the exact same trajectory. The same effect can also be achieved if $R_{s,x}$ and $R_{s,z}$ are both reduced to half with a doubling in scan time to cover the same FOV. However, in both cases, the off-trajectory points will not benefit from this seeming increase in density. In contrast, if only $R_{s,z}$ is reduced to half with a doubling in scan time, the trajectory itself will have twice as many triangles covering the same FOV. This time, the increased density will benefit the entire scanned FOV. Furthermore, the differences in scan time also need to be considered for a fair comparison of trajectories with respect to the noise level, as previously done in a thorough trajectory analysis of SFR-based image reconstruction [136]. Note that the color MPI simulations in Fig. 3.12 were noise-free and the experiments in Fig. 3.13 were performed using relatively high MNP concentrations showing negligible noise. Therefore, the differences in scan times did not cause any unfair bias in performance evaluations in this work.

3.6.5 Hardware and Safety Constraints on SR

In human-size applications of rapid TAURUS, both hardware and safety constraints will affect the imaging speed. The large imaging bore needed for human-size MPI scanners can require coils with large inductances [96, 137], with FF coil inductances in the mH range [138]. These large inductances can in turn limit the applicable SR, necessitating hardware solutions to reduce the inductances [139]. For FF safety limits, the 20 T/s safety limit of MRI gradient fields [89] was adopted, given the similarity of their operating frequencies. In MPI, the dominating safety constraint for both DF and FF is magnetostimulation [81]. During simultaneous application of DF and FF, the safety limits and the allowable SR for FF can further reduce [82]. Therefore, 20 T/s can be considered as an upper limit for the SR of FF. Note that while the limitations on SR can hinder the imaging speed of MPI in general, they in turn make the speed assumption in Eq. (3.17) easier to satisfy.

3.6.6 Extension to Other Rapid MPI Trajectories

This work utilized constant SRs in both the simulations and the experiments. In fact, a constant but high SR (e.g., 20 T/s) is the worst-case scenario for FF-induced distortions. If the assumption in Eq. (3.17) is satisfied, extending the proposed method to time-varying SRs should not pose a challenge.

In this work, a 1D DF was utilized. Trajectories with multi-dimensional DFs, such as the Lissajous trajectory, can cover a 2D/3D pFOV in a relatively short scan time [136]. For such trajectories, the assumption in Eq. (3.17) has to be satisfied for each DF axis. Since TAURUS requires a back-and-forth scanning, the multi-dimensional DFs may need to be applied twice, once forward and once backward [114]. Note that, while x-space reconstruction was previously proposed for such trajectories [126], an experimental demonstration is yet to be shown.

3.6.7 Signal-to-Noise Ratio and Clinical Applicability

For the noise robustness simulations in this work, the STD of the added noise was calculated using the peak signal amplitude before the direct feedthrough filtering (i.e., filtering of the first harmonic). However, the rapid TAURUS method was applied after the direct feedthrough filtering. Therefore, the SNR of the signal utilized in the τ estimations was in fact lower than the reported value. Considering this fact together with the results in Fig. 3.11, the proposed rapid TAURUS method is expected to be robust even at very low SNR levels.

In clinical applications, the administered particle concentrations are expected to be low, always imposing a boundary on *in vivo* SNR, since the iron concentration and corresponding MPI signal have a linear relationship. Detecting picogram levels of iron content has been shown to be possible using specialized equipment in *in vivo* mice experiments [97] and for stem cell tracking applications [71]. There are several opportunities to increase sensitivity, i.e., to reduce the minimum detectable iron content. For example, for the in-house MPI scanner used in this work, the primary source of noise was the low-noise amplifier in the receive chain. SNR is expected to increase substantially with specialized preamplifiers with lower noise figures, resulting in lower requirements for particle concentrations [140, 97]. Additionally, several scans can be averaged to improve the SNR by a factor of the square root of the number of averages at the expense of total scan time. Considering the possibility of real-time applications of rapid TAURUS, signal averaging will result in lower frame rates. However, such a trade-off can be considered depending on the application's requirements. Another method could be to use tailored MPI tracers that result in higher MPI signals. Tailored MPI tracers can reduce the required concentration for the same SNR [131, 141].

Chapter 4

Feasibility of Rapid TAURUS for Real-Time Color MPI

This chapter is based on the following publication:

- M.T. Arslan, and E. U. Saritas, “Rapid TAURUS for Real-Time Color MPI: A Feasibility Study,” in International Journal on Magnetic Particle Imaging, 2022, DOI: 10.18416/IJMPI.2022.2203060.

4.1 Introduction

Real-time color MPI can provide a safe alternative to x-ray fluoroscopy for catheter tracking during cardiovascular interventions [92], and a fast alternative to magnetic resonance imaging for the diagnosis of stroke [93].

TAURUS was previously proposed for relaxation-based color MPI [114, 104]. This thesis proposed rapid TAURUS to boost the performance of TAURUS to make it applicable for rapid and multi-dimensional trajectories [142]. Rapid

TAURUS utilizes time-varying FFs to rapidly scan a FOV, and corrects the FF-induced distortions on the signal before estimating the effective relaxation time constant, τ [142].

This chapter presents the first simulation results for real-time color MPI using rapid TAURUS. For a 5×6 cm^2 FOV. Frame rates exceeding 5 frames-per-second (FPS) are demonstrated. Higher frames can be achieved by zooming into a smaller region of interest (ROI). The results demonstrate the feasibility of real-time color MPI using rapid TAURUS.

4.2 Rapid TAURUS for Real-Time Color MPI

Figure 4.1 shows an example 2D triangle trajectory used for real-time color MPI adaptation of rapid TAURUS. A triangle shaped FF along the x-direction and a linearly ramping FF along the z-direction is utilized:

$$\boldsymbol{x}_s(t) = \begin{bmatrix} \frac{\mathrm{FOV}_x}{\pi} sin^{-1}\big(sin(2\pi f_{\mathsf{T}} t)\big) \\ 0 \\ \frac{R_{s,z} t}{G_z} \end{bmatrix} + \begin{bmatrix} 0 \\ 0 \\ \frac{B_p}{G_z} cos(2\pi f_d t) \end{bmatrix}. \tag{4.1}$$

Here, $\boldsymbol{x}_s(t)$ is the FFP position, $f_{\mathsf{T}} = R_{s,x}/(2\mathrm{FOV}_x G_x)$ is the frequency of the triangle wave, and B_p and f_d are the amplitude and frequency of the DF along the z-direction, respectively. In addition, $R_{s,i}$ (T/s) is the SR of the FF, G_i is the selection field gradient, and FOV_i is the FOV along direction i. The total scan time per frame is equal to $T_s = \mathrm{FOV}_z G_z / R_{s,z}$. The frame rate is then $\mathrm{FPS} = T_s^{-1}$.

Due to time-varying FFs, the FFP movement is not symmetrical around pFOV centers. This movement causes an additional distortion in the mirror symmetry of the signal, even for the adiabatic case of $\tau = 0$. Assuming that the FFP speed is dominated by the DF, the FF-induced distortion can be modeled as a time shift and an amplitude scaling between the two half cycles of a signal [142]. After distortion correction, τ was computed for each pFOV using TAURUS, by recovering the underlying mirror symmetry between the two half cycles of a DF period of the signal [114].

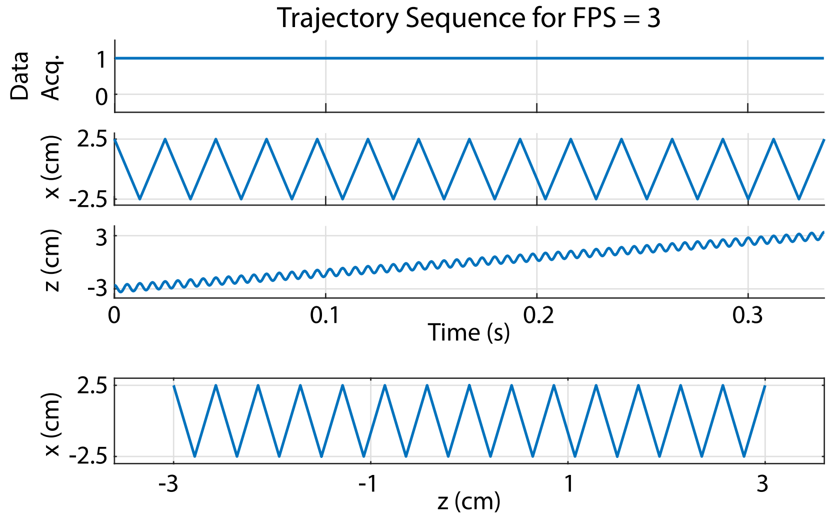

Figure 4.1: An example 2D trajectory for the case of FPS = 3. The trajectory covers a 5 × 6 cm^2 FOV. A triangle-wave motion along the x-direction, a linear motion along the z-direction, and a DF along the z-direction are utilized.

4.3 Simulations

The simulations were carried out using a custom toolbox in MATLAB (Mathworks, Natick, MA), using the following parameters: $(G_x, G_y, G_z) = (-4.8,\ 2.4,\ 2.4)$ T/m, $f_d = 20$ kHz, and $B_p = 10$ mT. The MNP responses were generated at 50 MS/s, and then downsampled to 2 MS/s. A zero-phase finite impulse response band-pass filter with the low and high cut-off frequencies of $1.5f_d$ and $10.5f_d$ was utilized for simultaneous direct feed-through filtering and high frequency noise removal. The flow diagram of the signal processing steps are given in Fig. 3.8.(b).

In Fig. 4.2.(a), the 5 × 6 cm^2 vasculature phantom used in the simulations is shown. The vessel structure had ≥2.5 mm diameter around the main branch and the catheter had 0.83 mm diameter. The relaxation effects were incorporated using the phenomenological model in [109]. The vessel structure contained MNPs with $\tau = 4$ μs and the catheter was labeled with MNPs that had $\tau = 2$ μs. Single-core monodisperse MNPs with 25 nm core diameter were assumed.

Two different simulations were performed. In the first simulation, the performances at three different FPS levels were compared for a 5×6 cm^2 FOV. FPS levels of 3, 4.2, and 7 were achieved by setting $R_{s,z}$ to 0.43, 0.6, and 1 T/s, respectively. In the second simulation, a reduced FOV of 2.5×3 cm^2 was scanned to zoom into a smaller ROI. A higher FPS level of 9.25 was achieved by setting $R_{s,z}$ to 0.7 T/s. In all of the simulations, $R_{s,x}$ was 20 T/s.

Image reconstruction consisted of three steps: First, Harmonic Dispersion X-space (HD-X) reconstruction was utilized to reconstruct the MPI images [132]. Because the data points from the 2D triangle trajectory were on a non-Cartesian grid, an automated gridding algorithm for non-Cartesian x-space reconstruction was adapted on the HD-X data [126]. Next, FF-induced time-shift and amplitude scaling distortions were corrected [142]. TAURUS was then applied for each DF period and the estimated τ value was placed on the corresponding pFOV center location to form a non-Cartesian τ map. The aforementioned gridding algorithm was utilized to reconstruct the Cartesian τ map. Finally, the color MPI image was generated by overlaying the τ map with the MPI image.

4.4 Results

Figure 4.2 shows the results for the FPS levels of 3, 4.2, and 7. The labeled catheter can be easily distinguished in the color overlay images at all FPS levels tested. In Fig. 4.2.(c), rapid TAURUS estimates τ within the vasculature structure as 4 μs. On the other hand, τ for the labeled catheter is estimated as 3.4 μs, which is higher than the original 2 μs. This result is expected, since TAURUS estimates a weighted average τ in regions that contain a mixture of MNPs with different τ values, as explained in [114].

As seen in Fig. 4.2, the fidelity of both the MPI image and the color overlay decreases with FPS. This result is a direct consequence of the reduced trajectory density at higher FPS levels. Note that the trajectory density is a function of the SRs due to Eq. (4.1). Increasing the FPS requires $R_{s,z}$ to be increased. To

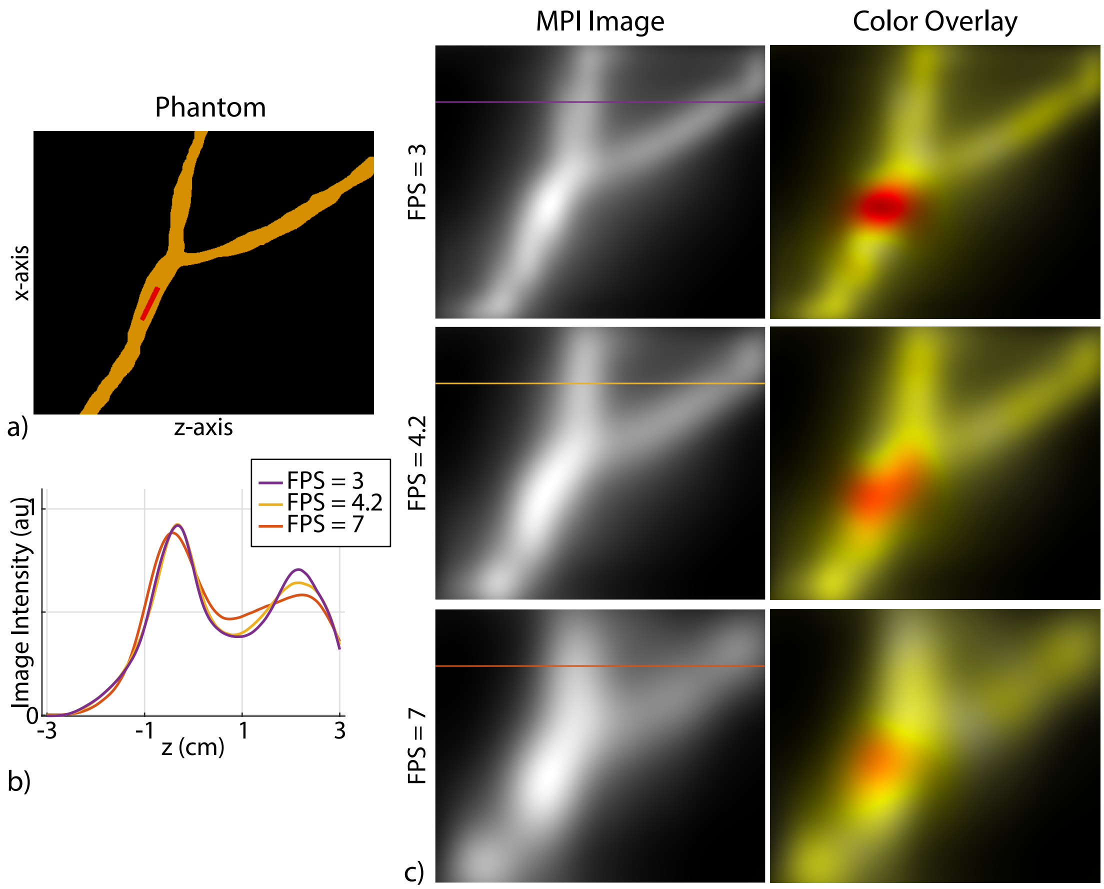

Figure 4.2: Color MPI simulation results. (a) The vasculature phantom containing a labeled catheter. (b) 1D cross-sections of MPI images at different FPS levels. (c) MPI images and color overlays for FPS = 3, 4.2, and 7. The colored lines mark the 1D cross-sections shown in (b). The labeled catheter can be easily distinguished in the color overlay images at all FPS levels.

maintain trajectory density and image resolution, $R_{s,x}$ would have to be increased at the same rate as $R_{s,z}$. In this work, $R_{s,x}$ was fixed to 20 T/s considering potential hardware and safety limitations With $R_{s,x}$ fixed, higher FPS levels resulted in reduced trajectory density, and thereby reduced image resolution.

Figure 4.3 shows that higher FPS levels can be achieved by zooming into a smaller ROI (chosen manually in this case). In Fig. 4.3.(a), first, the 5 × 6 cm^2 FOV was scanned at 3 FPS to locate the catheter tip. In Fig. 4.3.(b), a reduced FOV of 2.5 × 3 cm^2 was scanned at 9.25 FPS, resulting in a slightly higher resolution image with more than 3 times the FPS.

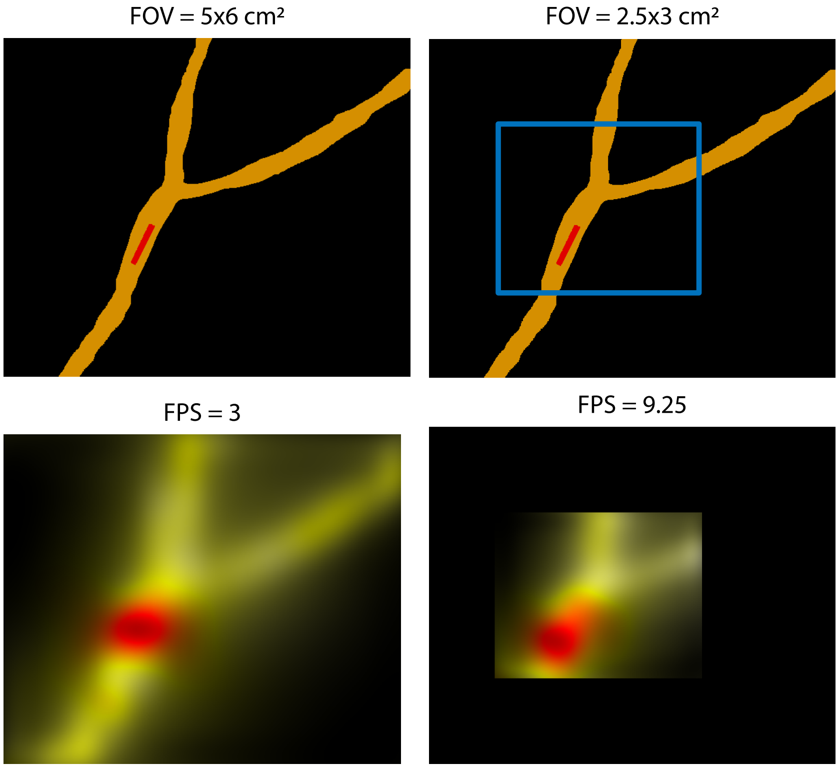

Figure 4.3: Color MPI simulation results at a higher FPS level for a zoomed-in ROI. Color overlay images are shown for (a) 5×6 cm^2 FOV imaged at FPS = 3 and (b) a reduced FOV of 2.5×3 cm^2 imaged at FPS = 9.25.

4.5 Discussion

For the real-time application, image reconstruction should be faster than T_s. For a single DF period, the average execution time of rapid TAURUS followed by τ map gridding was 0.75 ms, and that of HD-X followed by gridding was 0.6 ms, on an Intel i5-10600k with Windows 10. Considering that $f_d = 20$ kHz, the execution time per period corresponds to approximately 15 periods. Rapid TAURUS, HD-X, and gridding only require the individual DF periods and can be parallelized to run on different processor cores or a GPU for each DF period. Additionally, τ map generation and image reconstruction are completely separate processes. Therefore, an efficient implementation in a different programming language and parallelization can enable real-time reconstruction.

Chapter 5

Conclusion and Future Work

5.1 Conclusion

In this thesis, a novel SR correction method to compensate for the FF-induced distortions in the underlying mirror symmetry of the MPI signal was proposed. The proposed method depends only on the system and scanning parameters, and enables high-fidelity relaxation map estimations via TAURUS for rapid and multi-dimensional trajectories. The performance is further boosted via a weighted least squares approach. The results show robustness against a wide range of SRs and noise, together with orders of magnitude reduction in scan time. The proposed rapid relaxation mapping method will have important applications in developing the functional imaging capabilities of MPI.

Furthermore, in this thesis, the first simulation results demonstrating the feasibility of real-time color MPI via rapid TAURUS was shown. The results show that color MPI images can be successfully generated for a relatively wide FOV at frame rates exceeding 5 FPS. Additionally, a smaller ROI can be scanned at frame rates exceeding 9 FPS, without sacrificing from image fidelity. The analysis of the methods indicate that real-time reconstruction of both the $\hat{\tau}$ map and the MPI image are readily possible indicating that rapid TAURUS is an effective method for real-time color MPI.

The main disadvantage of the original TAURUS for x-space-based color MPI was the requirement of long scan times due to slow FFP trajectories. This requirement has been overcome with the novel method presented in this thesis. TAURUS can now be adapted to a wide variety of MPI scan sequences with possibilities of real-time applications.

5.2 Future Work

Controlling the trajectory density in a systematic fashion is challenging for 2DTT, as the trajectory parameters are coupled. Considering this coupling between the scan parameters, the effects of trajectory density on $\hat{\tau}$ map fidelity must be analyzed thoroughly with an appropriate definition of density, which remains an important future work.

Additionally, the main trajectory movement in this thesis was achieved through the modification of FF. On the other hand, trajectories with multi-dimensional DFs, such as the Lissajous trajectory, can cover a 2D/3D pFOV in a relatively short scan time and are commonly implemented, especially in systems that use SFR. X-space reconstruction was previously proposed for such trajectories, but an experimental demonstration is not presented yet. Extending TAURUS and x-space reconstruction to such multi-dimensional DFs remains an important future work.

The methods presented in this thesis were implemented in a custom toolbox implemented in MATLAB. As mentioned earlier, image reconstruction should be faster than the scanning sequence for real-time imaging applications. For a proper evaluation of the color MPI reconstruction speed, the presented algorithms must be implemented efficiently and possible parallelization opportunities must be exploited, which remain to be investigated.

Finally, in this thesis, the imaging experiments were conducted using an in-house MPI scanner. Due to the hardware limitations of this scanner, the FFs were realized through the mechanical movement of the phantom, which limited the slew rates substantially. The presented experimental work clearly shows the promise of the proposed rapid TAURUS method, and the experimental results are consistent with the simulation work. With that said, to achieve high slew rates in an experimental setting, the FFs should be implemented using magnetic field generating coils with relatively low inductance. Such an MPI system would be suitable to demonstrate the full potential of the proposed rapid TAURUS method for relaxation mapping, as well as for real-time imaging applications.

Bibliography

[1] S. C. Deoni, T. M. Peters, and B. K. Rutt, "High-resolution t1 and t2 mapping of the brain in a clinically acceptable time with despot1 and despot2," *Magnetic Resonance in Medicine: An Official Journal of the International Society for Magnetic Resonance in Medicine*, vol. 53, no. 1, pp. 237–241, 2005.

[2] P. K. Kim, Y. J. Hong, D. J. Im, Y. J. Suh, C. H. Park, J. Y. Kim, S. Chang, H.-J. Lee, J. Hur, Y. J. Kim, *et al.*, "Myocardial t1 and t2 mapping: techniques and clinical applications," *Korean journal of radiology*, vol. 18, no. 1, pp. 113–131, 2017.

[3] D. R. Messroghli, J. C. Moon, V. M. Ferreira, L. Grosse-Wortmann, T. He, P. Kellman, J. Mascherbauer, R. Nezafat, M. Salerno, E. B. Schelbert, *et al.*, "Clinical recommendations for cardiovascular magnetic resonance mapping of t1, t2, t2* and extracellular volume: a consensus statement by the society for cardiovascular magnetic resonance (scmr) endorsed by the european association for cardiovascular imaging (eacvi)," *Journal of Cardiovascular Magnetic Resonance*, vol. 19, no. 1, pp. 1–24, 2017.

[4] D. H. Hoffman, A. Ayoola, D. Nickel, F. Han, H. Chandarana, and K. P. Shanbhogue, "T1 mapping, t2 mapping and mr elastography of the liver for detection and staging of liver fibrosis," *Abdominal Radiology*, vol. 45, no. 3, pp. 692–700, 2020.

[5] D. Le Bihan, "Diffusion mri: what water tells us about the brain," *EMBO molecular medicine*, vol. 6, no. 5, pp. 569–573, 2014.

[6] V. Baliyan, C. J. Das, R. Sharma, and A. K. Gupta, "Diffusion weighted imaging: technique and applications," *World journal of radiology*, vol. 8, no. 9, p. 785, 2016.

[7] D. Le Bihan, J.-F. Mangin, C. Poupon, C. A. Clark, S. Pappata, N. Molko, and H. Chabriat, "Diffusion tensor imaging: concepts and applications," *Journal of Magnetic Resonance Imaging: An Official Journal of the International Society for Magnetic Resonance in Medicine*, vol. 13, no. 4, pp. 534–546, 2001.

[8] J.-D. Tournier, S. Mori, and A. Leemans, "Diffusion tensor imaging and beyond," *Magnetic resonance in medicine*, vol. 65, no. 6, p. 1532, 2011.

[9] H. Hanyu, H. Sakurai, T. Iwamoto, M. Takasaki, H. Shindo, and K. Abe, "Diffusion-weighted mr imaging of the hippocampus and temporal white matter in alzheimer's disease," *Journal of the neurological sciences*, vol. 156, no. 2, pp. 195–200, 1998.

[10] S. Warach, D. Chien, W. Li, M. Ronthal, and R. Edelman, "Fast magnetic resonance diffusion-weighted imaging of acute human stroke," *Neurology*, vol. 42, no. 9, pp. 1717–1717, 1992.

[11] A. Tanimoto, J. Nakashima, H. Kohno, H. Shinmoto, and S. Kuribayashi, "Prostate cancer screening: the clinical value of diffusion-weighted imaging and dynamic mr imaging in combination with t2-weighted imaging," *Journal of Magnetic Resonance Imaging: An Official Journal of the International Society for Magnetic Resonance in Medicine*, vol. 25, no. 1, pp. 146–152, 2007.

[12] A. R. Padhani, G. Liu, D. Mu-Koh, T. L. Chenevert, H. C. Thoeny, T. Takahara, A. Dzik-Jurasz, B. D. Ross, M. Van Cauteren, D. Collins, *et al.*, "Diffusion-weighted magnetic resonance imaging as a cancer biomarker: consensus and recommendations," *Neoplasia*, vol. 11, no. 2, pp. 102–125, 2009.

[13] P. M. Matthews and P. Jezzard, "Functional magnetic resonance imaging," *Journal of Neurology, Neurosurgery & Psychiatry*, vol. 75, no. 1, pp. 6–12, 2004.

[14] S. C. Cramer, G. Nelles, R. R. Benson, J. D. Kaplan, R. A. Parker, K. K. Kwong, D. N. Kennedy, S. P. Finklestein, and B. R. Rosen, "A functional mri study of subjects recovered from hemiparetic stroke," *Stroke*, vol. 28, no. 12, pp. 2518–2527, 1997.

[15] Y. Cao, L. D'olhaberriague, E. Vikingstad, S. Levine, and K. Welch, "Pilot study of functional mri to assess cerebral activation of motor function after poststroke hemiparesis," *Stroke*, vol. 29, no. 1, pp. 112–122, 1998.

[16] S. Y. Bookheimer, M. H. Strojwas, M. S. Cohen, A. M. Saunders, M. A. Pericak-Vance, J. C. Mazziotta, and G. W. Small, "Patterns of brain activation in people at risk for alzheimer's disease," *New England journal of medicine*, vol. 343, no. 7, pp. 450–456, 2000.

[17] M. A. Rocca and M. Filippi, "Functional mri in multiple sclerosis," *Journal of Neuroimaging*, vol. 17, pp. 36S–41S, 2007.

[18] J. E. Adcock, R. G. Wise, J. Oxbury, S. Oxbury, and P. M. Matthews, "Quantitative fmri assessment of the differences in lateralization of language-related brain activation in patients with temporal lobe epilepsy," *Neuroimage*, vol. 18, no. 2, pp. 423–438, 2003.

[19] W. T. Dixon, "Simple proton spectroscopic imaging.," *Radiology*, vol. 153, no. 1, pp. 189–194, 1984.

[20] R. J. Gillies and D. L. Morse, "In vivo magnetic resonance spectroscopy in cancer," *Annu. Rev. Biomed. Eng.*, vol. 7, pp. 287–326, 2005.

[21] S. K. Gujar, S. Maheshwari, I. Björkman-Burtscher, and P. C. Sundgren, "Magnetic resonance spectroscopy," *Journal of neuro-ophthalmology*, vol. 25, no. 3, pp. 217–226, 2005.

[22] N. Shah, A. Sattar, M. Benanti, S. Hollander, and L. Cheuck, "Magnetic resonance spectroscopy as an imaging tool for cancer: a review of the literature," *Journal of Osteopathic Medicine*, vol. 106, no. 1, pp. 23–27, 2006.

[23] C. J. Holloway, J. Suttie, S. Dass, and S. Neubauer, "Clinical cardiac magnetic resonance spectroscopy," *Progress in cardiovascular diseases*, vol. 54, no. 3, pp. 320–327, 2011.

[24] M. H. Buonocore and R. J. Maddock, "Magnetic resonance spectroscopy of the brain: a review of physical principles and technical methods," *Reviews in the Neurosciences*, vol. 26, no. 6, pp. 609–632, 2015.

[25] J. A. Stanley and N. Raz, "Functional magnetic resonance spectroscopy: the "new" mrs for cognitive neuroscience and psychiatry research," *Frontiers in psychiatry*, vol. 9, p. 76, 2018.

[26] C. H. Thng, T. San Koh, D. J. Collins, and D. M. Koh, "Perfusion magnetic resonance imaging of the liver," *World Journal of Gastroenterology: WJG*, vol. 16, no. 13, p. 1598, 2010.

[27] J. Keupp, J. Rahmer, I. Grässlin, P. C. Mazurkewitz, T. Schaeffter, G. M. Lanza, S. A. Wickline, and S. D. Caruthers, "Simultaneous dual-nuclei imaging for motion corrected detection and quantification of 19f imaging agents," *Magnetic resonance in medicine*, vol. 66, no. 4, pp. 1116–1122, 2011.

[28] I. Tirotta, V. Dichiarante, C. Pigliacelli, G. Cavallo, G. Terraneo, F. B. Bombelli, P. Metrangolo, and G. Resnati, "19f magnetic resonance imaging (mri): from design of materials to clinical applications," *Chemical reviews*, vol. 115, no. 2, pp. 1106–1129, 2015.

[29] R. Rutherford, B. Pullan, and I. Isherwood, "X-ray energies for effective atomic number determination," *Neuroradiology*, vol. 11, no. 1, pp. 23–28, 1976.

[30] R. E. Alvarez and A. Macovski, "Energy-selective reconstructions in x-ray computerised tomography," *Physics in Medicine & Biology*, vol. 21, no. 5, p. 733, 1976.

[31] T. G. Flohr, C. H. McCollough, H. Bruder, M. Petersilka, K. Gruber, C. Süβ, M. Grasruck, K. Stierstorfer, B. Krauss, R. Raupach, *et al.*, "First performance evaluation of a dual-source ct (dsct) system," *European radiology*, vol. 16, no. 2, pp. 256–268, 2006.

[32] T. R. Johnson, B. Krauss, M. Sedlmair, M. Grasruck, H. Bruder, D. Morhard, C. Fink, S. Weckbach, M. Lenhard, B. Schmidt, *et al.*, "Material differentiation by dual energy ct: initial experience," *European radiology*, vol. 17, no. 6, pp. 1510–1517, 2007.

[33] D. Marin, R. C. Nelson, E. Samei, E. K. Paulson, L. M. Ho, D. T. Boll, D. M. DeLong, T. T. Yoshizumi, and S. T. Schindera, "Hypervascular liver tumors: low tube voltage, high tube current multidetector ct during late hepatic arterial phase for detection—initial clinical experience," *Radiology*, vol. 251, no. 3, pp. 771–779, 2009.

[34] G. Schmid-Bindert, T. Henzler, T. Chu, M. Meyer, J. Nance, U. Schoepf, D. Dinter, P. Apfaltrer, R. Krissak, C. Manegold, *et al.*, "Functional imaging of lung cancer using dual energy ct: how does iodine related attenuation correlate with standardized uptake value of 18fdg-pet-ct?," *European radiology*, vol. 22, no. 1, pp. 93–103, 2012.

[35] L. Volterrani, F. Gentili, A. Fausto, V. Pelini, T. Megha, F. Sardanelli, and M. A. Mazzei, "Dual-energy ct for locoregional staging of breast cancer: preliminary results," *American Journal of Roentgenology*, vol. 214, no. 3, pp. 707–714, 2020.

[36] G. M. Lu, Y. Zhao, L. J. Zhang, and U. J. Schoepf, "Dual-energy ct of the lung," *American Journal of Roentgenology*, vol. 199, no. 5_supplement, pp. S40–S53, 2012.

[37] M. Karcaaltincaba and A. Aktas, "Dual-energy ct revisited with multidetector ct: review of principles and clinical applications," 2011.

[38] P. I. Mallinson, T. M. Coupal, P. D. McLaughlin, S. Nicolaou, P. L. Munk, and H. A. Ouellette, "Dual-energy ct for the musculoskeletal system," *Radiology*, vol. 281, no. 3, pp. 690–707, 2016.

[39] R. B. Schwartz, P. A. Carvalho, E. Alexander, J. Loeffler, R. Folkerth, and B. Holman, “Radiation necrosis vs high-grade recurrent glioma: differentiation by using dual-isotope spect with 201ti and 99mtc-hmpao.,” *American journal of neuroradiology*, vol. 12, no. 6, pp. 1187–1192, 1991.

[40] S. I. Heiba, D. Kolker, B. Mocherla, K. Kapoor, M. Jiang, H. Son, B. Rangaswamy, L. Kostakoglu, I. Savitch, M. DaCosta, *et al.*, “The optimized evaluation of diabetic foot infection by dual isotope spect/ct imaging protocol,” *The Journal of foot and ankle surgery*, vol. 49, no. 6, pp. 529–536, 2010.

[41] Y. Yamamoto, Y. Nishiyama, K. Satoh, Y. Ohbayashi, A. Iwasaki, K. Miyabe, and M. Ohkawa, “Dual-isotope spect using 99mtc-hydroxymethylene diphosphonate and 201tl-chloride to assess mandibular invasion by intraoral squamous cell carcinoma,” *Journal of Nuclear Medicine*, vol. 43, no. 11, pp. 1464–1468, 2002.

[42] D. Wagenaar, J. Zhang, T. Kazules, T. Vandehei, E. Bolle, S. Chowdhury, K. Parnham, and B. Patt, “In vivo dual-isotope spect imaging with improved energy resolution,” in *2006 IEEE Nuclear Science Symposium Conference Record*, vol. 6, pp. 3821–3826, IEEE, 2006.

[43] H. Kobayashi, M. R. Longmire, M. Ogawa, and P. L. Choyke, “Rational chemical design of the next generation of molecular imaging probes based on physics and biology: mixing modalities, colors and signals,” *Chemical Society Reviews*, vol. 40, no. 9, pp. 4626–4648, 2011.

[44] E. Tanaka, F. Y. Chen, R. Flaumenhaft, G. J. Graham, R. G. Laurence, and J. V. Frangioni, “Real-time assessment of cardiac perfusion, coronary angiography, and acute intravascular thrombi using dual-channel near-infrared fluorescence imaging,” *The Journal of thoracic and cardiovascular surgery*, vol. 138, no. 1, pp. 133–140, 2009.

[45] S. L. Troyan, V. Kianzad, S. L. Gibbs-Strauss, S. Gioux, A. Matsui, R. Oketokoun, L. Ngo, A. Khamene, F. Azar, and J. V. Frangioni, “The flare™ intraoperative near-infrared fluorescence imaging system: a first-in-human

clinical trial in breast cancer sentinel lymph node mapping," *Annals of surgical oncology*, vol. 16, no. 10, pp. 2943–2952, 2009.

[46] N. Kosaka, M. Ogawa, P. L. Choyke, and H. Kobayashi, "Clinical implications of near-infrared fluorescence imaging in cancer," *Future oncology*, vol. 5, no. 9, pp. 1501–1511, 2009.

[47] W. Cai, K. Chen, Z.-B. Li, S. S. Gambhir, and X. Chen, "Dual-function probe for pet and near-infrared fluorescence imaging of tumor vasculature," *Journal of Nuclear Medicine*, vol. 48, no. 11, pp. 1862–1870, 2007.

[48] H. Luo, C. G. England, S. Goel, S. A. Graves, F. Ai, B. Liu, C. P. Theuer, H. C. Wong, R. J. Nickles, and W. Cai, "Immunopet and near-infrared fluorescence imaging of pancreatic cancer with a dual-labeled bispecific antibody fragment," *Molecular pharmaceutics*, vol. 14, no. 5, pp. 1646–1655, 2017.

[49] B. T. Lee, A. Matsui, M. Hutteman, S. J. Lin, J. H. Winer, R. G. Laurence, and J. V. Frangioni, "Intraoperative near-infrared fluorescence imaging in perforator flap reconstruction: current research and early clinical experience," *Journal of reconstructive microsurgery*, vol. 26, no. 01, pp. 059–065, 2010.

[50] D. D. Adler, P. L. Carson, J. M. Rubin, and D. Quinn-Reid, "Doppler ultrasound color flow imaging in the study of breast cancer: preliminary findings," *Ultrasound in medicine & biology*, vol. 16, no. 6, pp. 553–559, 1990.

[51] T. H. Williamson and A. Harris, "Color doppler ultrasound imaging of theeye and orbit," *Survey of ophthalmology*, vol. 40, no. 4, pp. 255–267, 1996.

[52] K. Shimamoto, T. Endo, T. Ishigaki, S. Sakuma, and N. Makino, "Thyroid nodules: evaluation with color doppler ultrasonography," *Journal of ultrasound in medicine*, vol. 12, no. 11, pp. 673–678, 1993.

[53] A. W. Lensing, C. I. Doris, F. P. McGrath, A. Cogo, M. J. Sabine, J. Ginsberg, P. Prandoni, A. G. Turpie, and J. Hirsh, "A comparison of compression ultrasound with color doppler ultrasound for the diagnosis of symptomless postoperative deep vein thrombosis," *Archives of internal medicine*, vol. 157, no. 7, pp. 765–768, 1997.

[54] R. K. Chiou, J. C. Anderson, R. K. Wobig, D. E. Rosinsky, A. Matamoros Jr, W. S. Chen, and R. J. Taylor, "Color doppler ultrasound criteria to diagnose varicoceles: correlation of a new scoring system with physical examination," *Urology*, vol. 50, no. 6, pp. 953–956, 1997.

[55] E. d. O. Barcaui, A. C. P. Carvalho, F. P. P. L. Lopes, J. Piñeiro-Maceira, and C. B. Barcaui, "High frequency ultrasound with color doppler in dermatology," *Anais brasileiros de dermatologia*, vol. 91, pp. 262–273, 2016.

[56] S. A. Hilderbrand and R. Weissleder, "Near-infrared fluorescence: application to in vivo molecular imaging," *Current opinion in chemical biology*, vol. 14, no. 1, pp. 71–79, 2010.

[57] R. Weissleder and M. J. Pittet, "Imaging in the era of molecular oncology," *Nature*, vol. 452, no. 7187, pp. 580–589, 2008.

[58] C. Li and Q. Wang, "Challenges and opportunities for intravital near-infrared fluorescence imaging technology in the second transparency window," *ACS nano*, vol. 12, no. 10, pp. 9654–9659, 2018.

[59] S. Bjaerum, H. Torp, and K. Kristoffersen, "Clutter filters adapted to tissue motion in ultrasound color flow imaging," *IEEE transactions on ultrasonics, ferroelectrics, and frequency control*, vol. 49, no. 6, pp. 693–704, 2002.

[60] C. Alfred and L. Lovstakken, "Eigen-based clutter filter design for ultrasound color flow imaging: A review," *IEEE transactions on ultrasonics, ferroelectrics, and frequency control*, vol. 57, no. 5, pp. 1096–1111, 2010.

[61] D. W. Townsend, J. P. Carney, J. T. Yap, and N. C. Hall, "Pet/ct today and tomorrow," *Journal of Nuclear Medicine*, vol. 45, no. 1 suppl, pp. 4S–14S, 2004.

[62] J. Lohrke, T. Frenzel, J. Endrikat, F. C. Alves, T. M. Grist, M. Law, J. M. Lee, T. Leiner, K.-C. Li, K. Nikolaou, *et al.*, "25 years of contrast-enhanced mri: developments, current challenges and future perspectives," *Advances in therapy*, vol. 33, no. 1, pp. 1–28, 2016.

[63] T. Vita, D. R. Okada, M. Veillet-Chowdhury, P. E. Bravo, E. Mullins, E. Hulten, M. Agrawal, R. Madan, V. R. Taqueti, M. Steigner, *et al.*, "Complementary value of cardiac magnetic resonance imaging and positron emission tomography/computed tomography in the assessment of cardiac sarcoidosis," *Circulation: Cardiovascular Imaging*, vol. 11, no. 1, p. e007030, 2018.

[64] B. Gleich and J. Weizenecker, "Tomographic imaging using the nonlinear response of magnetic particles," *Nature*, vol. 435, no. 7046, pp. 1214–1217, 2005.

[65] P. W. Goodwill, E. U. Saritas, L. R. Croft, T. N. Kim, K. M. Krishnan, D. V. Schaffer, and S. M. Conolly, "X-space mpi: magnetic nanoparticles for safe medical imaging," *Advanced materials*, vol. 24, no. 28, pp. 3870–3877, 2012.

[66] E. U. Saritas, P. W. Goodwill, L. R. Croft, J. J. Konkle, K. Lu, B. Zheng, and S. M. Conolly, "Magnetic particle imaging (mpi) for nmr and mri researchers," *Journal of Magnetic Resonance*, vol. 229, pp. 116–126, 2013.

[67] B. Zheng, E. Yu, R. Orendorff, K. Lu, J. J. Konkle, Z. W. Tay, D. Hensley, X. Y. Zhou, P. Chandrasekharan, E. U. Saritas, *et al.*, "Seeing spios directly in vivo with magnetic particle imaging," *Molecular imaging and biology*, vol. 19, no. 3, pp. 385–390, 2017.

[68] L. Wu, Y. Zhang, G. Steinberg, H. Qu, S. Huang, M. Cheng, T. Bliss, F. Du, J. Rao, G. Song, *et al.*, "A review of magnetic particle imaging and perspectives on neuroimaging," *American Journal of Neuroradiology*, vol. 40, no. 2, pp. 206–212, 2019.

[69] I. Molwitz, H. Ittrich, T. Knopp, T. Mummert, J. Salamon, C. Jung, G. Adam, and M. Kaul, "First magnetic particle imaging angiography in

human-sized organs by employing a multimodal ex vivo pig kidney perfusion system," *Physiological measurement*, vol. 40, no. 10, p. 105002, 2019.

[70] A. Mohtashamdolatshahi, H. Kratz, O. Kosch, R. Hauptmann, N. Stolzenburg, F. Wiekhorst, I. Sack, B. Hamm, M. Taupitz, and J. Schnorr, "In vivo magnetic particle imaging: angiography of inferior vena cava and aorta in rats using newly developed multicore particles," *Scientific reports*, vol. 10, no. 1, pp. 1–9, 2020.

[71] B. Zheng, T. Vazin, P. W. Goodwill, A. Conway, A. Verma, E. U. Saritas, D. Schaffer, and S. M. Conolly, "Magnetic particle imaging tracks the long-term fate of in vivo neural cell implants with high image contrast," *Scientific reports*, vol. 5, no. 1, pp. 1–9, 2015.

[72] K. Them, J. Salamon, P. Szwargulski, S. Sequeira, M. Kaul, C. Lange, H. Ittrich, and T. Knopp, "Increasing the sensitivity for stem cell monitoring in system-function based magnetic particle imaging," *Physics in Medicine & Biology*, vol. 61, no. 9, p. 3279, 2016.

[73] Q. Wang, X. Ma, H. Liao, Z. Liang, F. Li, J. Tian, and D. Ling, "Artificially engineered cubic iron oxide nanoparticle as a high-performance magnetic particle imaging tracer for stem cell tracking," *ACS nano*, vol. 14, no. 2, pp. 2053–2062, 2020.

[74] D. B. Mangarova, J. Brangsch, A. Mohtashamdolatshahi, O. Kosch, H. Paysen, F. Wiekhorst, R. Klopfleisch, R. Buchholz, U. Karst, M. Taupitz, *et al.*, "Ex vivo magnetic particle imaging of vascular inflammation in abdominal aortic aneurysm in a murine model," *Scientific Reports*, vol. 10, no. 1, pp. 1–11, 2020.

[75] P. Chandrasekharan, K. B. Fung, X. Y. Zhou, W. Cui, C. Colson, D. Mai, K. Jeffris, Q. Huynh, C. Saayujya, L. Kabuli, *et al.*, "Non-radioactive and sensitive tracking of neutrophils towards inflammation using antibody functionalized magnetic particle imaging tracers," *Nanotheranostics*, vol. 5, no. 2, p. 240, 2021.

[76] Z. W. Tay, P. Chandrasekharan, X. Y. Zhou, E. Yu, B. Zheng, and S. Conolly, "In vivo tracking and quantification of inhaled aerosol using magnetic particle imaging towards inhaled therapeutic monitoring," *Theranostics*, vol. 8, no. 13, p. 3676, 2018.

[77] X. Zhu, J. Li, P. Peng, N. Hosseini Nassab, and B. R. Smith, "Quantitative drug release monitoring in tumors of living subjects by magnetic particle imaging nanocomposite," *Nano letters*, vol. 19, no. 10, pp. 6725–6733, 2019.

[78] R. Orendorff, A. J. Peck, B. Zheng, S. N. Shirazi, R. M. Ferguson, A. P. Khandhar, S. J. Kemp, P. Goodwill, K. M. Krishnan, G. A. Brooks, *et al.*, "First in vivo traumatic brain injury imaging via magnetic particle imaging," *Physics in Medicine & Biology*, vol. 62, no. 9, p. 3501, 2017.

[79] E. Y. Yu, M. Bishop, B. Zheng, R. M. Ferguson, A. P. Khandhar, S. J. Kemp, K. M. Krishnan, P. W. Goodwill, and S. M. Conolly, "Magnetic particle imaging: a novel in vivo imaging platform for cancer detection," *Nano letters*, vol. 17, no. 3, pp. 1648–1654, 2017.

[80] Z. W. Tay, P. Chandrasekharan, A. Chiu-Lam, D. W. Hensley, R. Dhavalikar, X. Y. Zhou, E. Y. Yu, P. W. Goodwill, B. Zheng, C. Rinaldi, *et al.*, "Magnetic particle imaging-guided heating in vivo using gradient fields for arbitrary localization of magnetic hyperthermia therapy," *ACS nano*, vol. 12, no. 4, pp. 3699–3713, 2018.

[81] E. U. Saritas, P. W. Goodwill, G. Z. Zhang, and S. M. Conolly, "Magnetostimulation limits in magnetic particle imaging," *IEEE transactions on medical imaging*, vol. 32, no. 9, pp. 1600–1610, 2013.

[82] I. Schmale, B. Gleich, J. Rahmer, C. Bontus, J. Schmidt, and J. Borgert, "Mpi safety in the view of mri safety standards," *IEEE Transactions on Magnetics*, vol. 51, no. 2, pp. 1–4, 2015.

[83] J. J. Konkle, P. W. Goodwill, E. U. Saritas, B. Zheng, K. Lu, and S. M. Conolly, "Twenty-fold acceleration of 3d projection reconstruction mpi," *Biomedizinische Technik/Biomedical Engineering*, vol. 58, no. 6, pp. 565–576, 2013.

[84] P. Aggarwal, J. B. Hall, C. B. McLeland, M. A. Dobrovolskaia, and S. E. McNeil, “Nanoparticle interaction with plasma proteins as it relates to particle biodistribution, biocompatibility and therapeutic efficacy,” *Advanced drug delivery reviews*, vol. 61, no. 6, pp. 428–437, 2009.

[85] N. Malhotra, J.-S. Lee, R. A. D. Liman, J. M. S. Ruallo, O. B. Villaflores, T.-R. Ger, and C.-D. Hsiao, “Potential toxicity of iron oxide magnetic nanoparticles: A review,” *Molecules*, vol. 25, no. 14, p. 3159, 2020.

[86] H. Markides, M. Rotherham, and A. El Haj, “Biocompatibility and toxicity of magnetic nanoparticles in regenerative medicine,” *Journal of Nanomaterials*, vol. 2012, 2012.

[87] E. U. Saritas, P. W. Goodwill, G. Z. Zhang, W. Yu, and S. M. Conolly, “Safety limits for human-size magnetic particle imaging systems,” in *Magnetic Particle Imaging*, pp. 325–330, Springer, 2012.

[88] N. Panagiotopoulos, R. L. Duschka, M. Ahlborg, G. Bringout, C. Debbeler, M. Graeser, C. Kaethner, K. Lüdtke-Buzug, H. Medimagh, J. Stelzner, *et al.*, “Magnetic particle imaging: current developments and future directions,” *International journal of nanomedicine*, vol. 10, p. 3097, 2015.

[89] International Commission on Non-Ionizing Radiation Protection, “Medical magnetic resonance (mr) procedures: protection of patients,” *Health Physics*, vol. 87, no. 2, pp. 197–216, 2004.

[90] J. Weizenecker, B. Gleich, J. Rahmer, H. Dahnke, and J. Borgert, “Three-dimensional real-time in vivo magnetic particle imaging,” *Physics in Medicine & Biology*, vol. 54, no. 5, p. L1, 2009.

[91] T.-A. Le, X. Zhang, A. K. Hoshiar, and J. Yoon, “Real-time two-dimensional magnetic particle imaging for electromagnetic navigation in targeted drug delivery,” *Sensors*, vol. 17, no. 9, p. 2050, 2017.

[92] J. Rahmer, D. Wirtz, C. Bontus, J. Borgert, and B. Gleich, “Interactive magnetic catheter steering with 3-d real-time feedback using multi-color magnetic particle imaging,” *IEEE transactions on medical imaging*, vol. 36, no. 7, pp. 1449–1456, 2017.

[93] P. Szwargulski, M. Wilmes, E. Javidi, F. Thieben, M. Graeser, M. Koch, C. Gruettner, G. Adam, C. Gerloff, T. Magnus, *et al.*, "Monitoring intracranial cerebral hemorrhage using multicontrast real-time magnetic particle imaging," *ACS nano*, vol. 14, no. 10, pp. 13913–13923, 2020.

[94] M. T. Arslan and E. U. Saritas, "Rapid taurus for real-time color mpi: A feasibility study," *International Journal on Magnetic Particle Imaging*, vol. 8, no. 1 Suppl 1, 2022.

[95] A. Meola, J. Rao, N. Chaudhary, G. Song, X. Zheng, and S. D. Chang, "Magnetic particle imaging in neurosurgery," *World neurosurgery*, vol. 125, pp. 261–270, 2019.

[96] E. E. Mason, C. Z. Cooley, S. F. Cauley, M. A. Griswold, S. M. Conolly, and L. L. Wald, "Design analysis of an mpi human functional brain scanner," *International journal on magnetic particle imaging*, vol. 3, no. 1, 2017.

[97] M. Graeser, P. Ludewig, P. Szwargulski, F. Foerger, T. Liebing, N. D. Forkert, F. Thieben, T. Magnus, and T. Knopp, "Design of a head coil for high resolution mouse brain perfusion imaging using magnetic particle imaging," *Physics in Medicine & Biology*, vol. 65, no. 23, p. 235007, 2020.

[98] A. A. Ozaslan, M. Utkur, U. Canpolat, M. A. Tuncer, K. K. Oguz, and E. U. Saritas, "Pns limits for human head-size mpi systems: Preliminary results," *International Journal on Magnetic Particle Imaging*, vol. 8, no. 1 Suppl 1, 2022.

[99] J. Rahmer, A. Halkola, B. Gleich, I. Schmale, and J. Borgert, "First experimental evidence of the feasibility of multi-color magnetic particle imaging," *Physics in Medicine & Biology*, vol. 60, no. 5, p. 1775, 2015.

[100] J. Haegele, S. Vaalma, N. Panagiotopoulos, J. Barkhausen, F. M. Vogt, J. Borgert, and J. Rahmer, "Multi-color magnetic particle imaging for cardiovascular interventions," *Physics in Medicine & Biology*, vol. 61, no. 16, p. N415, 2016.

[101] M. Utkur, Y. Muslu, and E. U. Saritas, “Relaxation-based viscosity mapping for magnetic particle imaging,” *Physics in Medicine & Biology*, vol. 62, no. 9, p. 3422, 2017.

[102] C. Shasha, E. Teeman, and K. M. Krishnan, “Harmonic simulation study of simultaneous nanoparticle size and viscosity differentiation,” *IEEE Magnetics Letters*, vol. 8, pp. 1–5, 2017.

[103] M. Möddel, C. Meins, J. Dieckhoff, and T. Knopp, “Viscosity quantification using multi-contrast magnetic particle imaging,” *New journal of physics*, vol. 20, no. 8, p. 083001, 2018.

[104] M. Utkur, Y. Muslu, and E. Saritas, “Relaxation-based color magnetic particle imaging for viscosity mapping,” *Applied Physics Letters*, vol. 115, no. 15, p. 152403, 2019.

[105] S. Draack, M. Schilling, and T. Viereck, “Magnetic particle imaging of particle dynamics in complex matrix systems,” *Physical Sciences Reviews*, 2021.

[106] C. Stehning, B. Gleich, and J. Rahmer, “Simultaneous magnetic particle imaging (mpi) and temperature mapping using multi-color mpi,” *International Journal on Magnetic Particle Imaging*, vol. 2, no. 2, 2016.

[107] J. Zhong, M. Schilling, and F. Ludwig, “Magnetic nanoparticle temperature imaging with a scanning magnetic particle spectrometer,” *Measurement Science and Technology*, vol. 29, no. 11, p. 115903, 2018.

[108] Y. Shi and J. B. Weaver, “Concurrent quantification of magnetic nanoparticles temperature and relaxation time,” *Medical physics*, vol. 46, no. 9, pp. 4070–4076, 2019.

[109] L. R. Croft, P. W. Goodwill, and S. M. Conolly, “Relaxation in x-space magnetic particle imaging,” *IEEE transactions on medical imaging*, vol. 31, no. 12, pp. 2335–2342, 2012.

[110] J. Rahmer, J. Weizenecker, B. Gleich, and J. Borgert, “Signal encoding in magnetic particle imaging: properties of the system function,” *BMC medical imaging*, vol. 9, no. 1, pp. 1–21, 2009.

[111] J. Rahmer, J. Weizenecker, B. Gleich, and J. Borgert, “Analysis of a 3-d system function measured for magnetic particle imaging,” *IEEE transactions on medical imaging*, vol. 31, no. 6, pp. 1289–1299, 2012.

[112] P. W. Goodwill and S. M. Conolly, “The x-space formulation of the magnetic particle imaging process: 1-d signal, resolution, bandwidth, snr, sar, and magnetostimulation,” *IEEE transactions on medical imaging*, vol. 29, no. 11, pp. 1851–1859, 2010.

[113] D. Hensley, P. Goodwill, L. Croft, and S. Conolly, “Preliminary experimental x-space color mpi,” in *2015 5th International Workshop on Magnetic Particle Imaging (IWMPI)*, pp. 1–1, IEEE, 2015.

[114] Y. Muslu, M. Utkur, O. B. Demirel, and E. U. Saritas, “Calibration-free relaxation-based multi-color magnetic particle imaging,” *IEEE transactions on medical imaging*, vol. 37, no. 8, pp. 1920–1931, 2018.

[115] S. Achenbach, “Computed tomography coronary angiography,” *Journal of the American College of Cardiology*, vol. 48, no. 10, pp. 1919–1928, 2006.

[116] J. J. Kim and A. D. Gean, “Imaging for the diagnosis and management of traumatic brain injury,” *Neurotherapeutics*, vol. 8, no. 1, pp. 39–53, 2011.

[117] M. Ütkür, *Cancer imaging and treatment monitoring with color magnetic particle imaging*. PhD thesis, Bilkent University, 2021.

[118] J. P. Bullivant, S. Zhao, B. J. Willenberg, B. Kozissnik, C. D. Batich, and J. Dobson, “Materials characterization of feraheme/ferumoxytol and preliminary evaluation of its potential for magnetic fluid hyperthermia,” *International journal of molecular sciences*, vol. 14, no. 9, pp. 17501–17510, 2013.

[119] P. Reimer and T. Balzer, “Ferucarbotran (resovist): a new clinically approved res-specific contrast agent for contrast-enhanced mri of the liver:

properties, clinical development, and applications," *European radiology*, vol. 13, no. 6, pp. 1266–1276, 2003.

[120] T. Knopp and T. M. Buzug, *Magnetic particle imaging: an introduction to imaging principles and scanner instrumentation.* Springer Science & Business Media, 2012.

[121] P. W. Goodwill and S. M. Conolly, "Multidimensional x-space magnetic particle imaging," *IEEE transactions on medical imaging*, vol. 30, no. 9, pp. 1581–1590, 2011.

[122] M. Gruettner, M. Graeser, S. Biederer, T. Sattel, H. Wojtczyk, W. Tenner, T. Knopp, B. Gleich, J. Borgert, and T. Buzug, "1d-image reconstruction for magnetic particle imaging using a hybrid system function," in *2011 IEEE Nuclear Science Symposium Conference Record*, pp. 2545–2548, IEEE, 2011.

[123] A. Halkola, J. Rahmer, B. Gleich, J. Borgert, and T. Buzug, "System calibration unit for magnetic particle imaging: system matrix," in *2013 International Workshop on Magnetic Particle Imaging (IWMPI)*, pp. 1–1, IEEE, 2013.

[124] M. Grüttner, T. Knopp, J. Franke, M. Heidenreich, J. Rahmer, A. Halkola, C. Kaethner, J. Borgert, and T. M. Buzug, "On the formulation of the image reconstruction problem in magnetic particle imaging," *Biomedizinische Technik/Biomedical Engineering*, vol. 58, no. 6, pp. 583–591, 2013.

[125] A. Von Gladiss, M. Gräser, P. Szwargulski, T. Knopp, and T. M. Buzug, "Hybrid system calibration for multidimensional magnetic particle imaging," *Physics in Medicine & Biology*, vol. 62, no. 9, p. 3392, 2017.

[126] A. Ozaslan, A. Alacaoglu, O. Demirel, T. Çukur, and E. Saritas, "Fully automated gridding reconstruction for non-cartesian x-space magnetic particle imaging," *Physics in Medicine & Biology*, vol. 64, no. 16, p. 165018, 2019.

[127] S. Kurt, Y. Muslu, and E. U. Saritas, "Partial fov center imaging (pci): a robust x-space image reconstruction for magnetic particle imaging," *IEEE Transactions on Medical Imaging*, vol. 39, no. 11, pp. 3441–3450, 2020.

[128] S. Ota and Y. Takemura, "Characterization of néel and brownian relaxations isolated from complex dynamics influenced by dipole interactions in magnetic nanoparticles," *The Journal of Physical Chemistry C*, vol. 123, no. 47, pp. 28859–28866, 2019.

[129] R. E. Rosensweig, "Heating magnetic fluid with alternating magnetic field," *Journal of magnetism and magnetic materials*, vol. 252, pp. 370–374, 2002.

[130] Z. W. Tay, D. W. Hensley, E. C. Vreeland, B. Zheng, and S. M. Conolly, "The relaxation wall: experimental limits to improving mpi spatial resolution by increasing nanoparticle core size," *Biomedical physics & engineering express*, vol. 3, no. 3, p. 035003, 2017.

[131] R. M. Ferguson, A. P. Khandhar, S. J. Kemp, H. Arami, E. U. Saritas, L. R. Croft, J. Konkle, P. W. Goodwill, A. Halkola, J. Rahmer, *et al.*, "Magnetic particle imaging with tailored iron oxide nanoparticle tracers," *IEEE transactions on medical imaging*, vol. 34, no. 5, pp. 1077–1084, 2014.

[132] S. Kurt, V. Abdulla, and E. U. Saritas, "Multi-dimensional harmonic dispersion x-space mpi," *International Journal on Magnetic Particle Imaging*, vol. 6, no. 2 Suppl 1, 2020.

[133] R. J. Hanisch, R. L. White, and R. L. Gilliland, "Deconvolution of hubbles space telescope images and spectra," in *Deconvolution of images and spectra (2nd ed.)*, pp. 310–360, 1996.

[134] D. Pantke, N. Holle, A. Mogarkar, M. Straub, and V. Schulz, "Multifrequency magnetic particle imaging enabled by a combined passive and active drive field feed-through compensation approach," *Medical Physics*, vol. 46, no. 9, pp. 4077–4086, 2019.

[135] B. Tasdelen, E. Yagiz, M. Utkur, A. R. Cagil, C. B. Top, E. Atalar, and E. U. Saritas, "Vector modulator based active compensation of direct

feedthrough," *International Journal on Magnetic Particle Imaging*, vol. 6, no. 2 Suppl 1, 2020.

[136] T. Knopp, S. Biederer, T. Sattel, J. Weizenecker, B. Gleich, J. Borgert, and T. Buzug, "Trajectory analysis for magnetic particle imaging," *Physics in Medicine & Biology*, vol. 54, no. 2, p. 385, 2008.

[137] M. Gräser, F. Thieben, P. Szwargulski, F. Werner, N. Gdaniec, M. Boberg, F. Griese, M. Möddel, P. Ludewig, D. van de Ven, *et al.*, "Human-sized magnetic particle imaging for brain applications," *Nature communications*, vol. 10, no. 1, pp. 1–9, 2019.

[138] C. B. Top, S. Ilbey, and H. E. Güven, "Electronically rotated and translated field-free line generation for open bore magnetic particle imaging," *Medical Physics*, vol. 44, no. 12, pp. 6225–6238, 2017.

[139] A. A. Ozaslan, A. R. Cagil, M. Graeser, T. Knopp, and E. U. Saritas, "Design of a magnetostimulation head coil with rutherford cable winding," *International Journal on Magnetic Particle Imaging*, vol. 6, no. 2 Suppl 1, 2020.

[140] W. Zhang, B. Zheng, P. Goodwill, and S. Conolly, "A custom low-noise preamplifier for magnetic particle imaging," in *2015 5th International Workshop on Magnetic Particle Imaging (IWMPI)*, pp. 1–1, IEEE, 2015.

[141] A. P. Khandhar, R. M. Ferguson, H. Arami, S. J. Kemp, and K. M. Krishnan, "Tuning surface coatings of optimized magnetite nanoparticle tracers for in vivo magnetic particle imaging," *IEEE transactions on magnetics*, vol. 51, no. 2, pp. 1–4, 2015.

[142] M. T. Arslan, A. A. Özaslan, S. Kurt, Y. Muslu, and E. U. Saritas, "Rapid taurus for relaxation-based color magnetic particle imaging," *IEEE Transactions on Medical Imaging*, 2022.